https://doi.org/10.5194/egusphere-2026-4270
Preprint. Discussion started: 23 July 2026


# Performance assessment of real-time earthquake localization algorithms for Earthquake Early Warning Systems in the Ibero-Maghrebian Region

Lucía Escudero[1], Maurizio Mattesini[1], Aldo Zollo[2], Grazia De Landro[2], Luca Elia[2,3], and Elisa Buforn[1]

[1] Department of Earth Physics and Astrophysics, Universidad Complutense de Madrid, 28040 Madrid, Spain.
[2] Department of Physics "*Ettore Pancini*", University of Naples Federico II, 80126 Naples, Italy.
[3] Osservatorio Vesuviano, National Institute of Geophysics and Volcanology, 80125 Naples, Italy.

*Correspondence to*: Lucía Escudero (lescud01@ucm.es)

**Abstract.** We evaluate the performance of two real-time earthquake location algorithms, *RTLoc* and *MParLoc*, implemented in the Earthquake Early Warning System (EEWS) *QuakeUp*. Specifically, we assess whether the recently developed *MParLoc* algorithm—which incorporates P-wave arrival times, P-peak amplitude ratios, and back-azimuth estimates—improves earthquake localization accuracy in the Ibero-Maghrebian Region (IMR). Analyzing $M_w \geq 4$ earthquakes recorded in the IMR between 2011 and 2026, we find that *MParLoc* generally outperforms *RTLoc*. It yields hypocentral locations significantly closer to reference solutions, particularly during the earliest stages after earthquake detection, when only a few stations and short P-wave windows are available. Although both methods converge as more P-wave picks accumulate, *MParLoc*'s early-stage precision is critical. Hypocentral accuracy strongly influences the distance term in the ground motion prediction equations used to generate real-time shakemaps, which define the spatial distribution of expected ground shaking and delineate Potential Damage Zones (PDZs). The results indicate that implementing *MParLoc* in PDZ-based EEWS like *QuakeUp* would significantly improve warning performance in the IMR, especially during the initial stages of an earthquake, by reducing the time to first alert, increasing lead-time for emergency safety actions, and providing valuable scientific and operational information for emergency response.

## 1 Introduction

Population growth and the increasing concentration of infrastructure in metropolitan areas have heightened society's vulnerability to earthquakes. Regardless of earthquake frequency, the exposure and interdependence of modern infrastructure and socioeconomic systems have intensified. Earthquake Early Warning Systems (EEWS) represent one of the most effective tools for reducing and mitigating earthquake-caused damage. EEWS evaluate the potentially damaging effects of an earthquake in real-time. When predefined thresholds are exceeded, they issue an early warning, enabling the initiation of emergency protocols or the evacuation of vulnerable areas before destructive seismic waves arrive. This advance notice

https://doi.org/10.5194/egusphere-2026-4270
Preprint. Discussion started: 23 July 2026


helps protect both the population and critical infrastructure while mitigating damage (Zollo et al., 2023; Rea et al., 2024; Escudero et al., 2025).

In network-based EEWS, the main task is the rapid detection of seismic events and the accurate determination of hypocentral coordinates and origin time (OT). These parameters are essential for assessing earthquake magnitude and predicting Potential Damage Zones (PDZ). They also allow estimation of the available lead-time — the time for emergency safety and security actions to protect the population, buildings, and industrial facilities before the onset of strong ground shaking — particularly for sensitive target infrastructures (Zollo et al., 2023; Rea et al., 2024; Escudero et al., 2025).

At any near-fault seismological observatory, determining an earthquake's hypocentral location is a routine task, typically completed a few minutes after the earthquake OT once most or all phase arrival times at the recording stations have been identified. However, when dealing with automatic EEWS applications, source parameters must be estimated within only a few seconds of the event detection. This constraint introduces the additional challenge of obtaining a reliable and stable solution despite a limited and often sparse set of early arrival-time data (Zollo et al., 2021). Currently, several approaches for real-time earthquake location have emerged, alongside a variety of parameters designed to better constrain the solution. These developments enable the construction of robust hypocentral solutions that are progressively refined as new data from stations increasingly distant from the seismic source become available (Zollo et al., 2021).

The first automatic real-time earthquake location methods were based on the progressive measurement of P-wave arrival times at stations located at increasing distances from the seismic source. Examples include the *ElarmS* methodology (Allen, 2007) and other approaches based on the *Equal Differential Time* (EDT, Font et al., 2004) surface (e.g., Horiuchi et al., 2005; Satriano et al., 2008). These methods were subsequently followed by other approaches that incorporated either single-station back-azimuth (BAZ) estimates (Noda et al., 2012; Eisermann et al., 2015) or the joint use of P and S-wave travel times and amplitudes to constrain the location of events occurring in an aftershock sequence (Liu and Yamada, 2014; Wu et al., 2015). More recently, Zollo et al., 2021proposed an evolutionary Bayesian method called *MParLoc* that exploits three different observables—differential P-wave arrival times (ΔTimes), P-peak amplitude ratios (ΔAmp), and back-azimuth (BAZ) estimates—measured within progressive (or fixed) time windows after the P-wave arrival.

In October 2015, the Department of Earth Physics and Astrophysics at *Universidad Complutense de Madrid* (UCM) in Spain deployed a network-based EEWS specifically tailored to the Ibero-Maghrebian Region (IMR) using the *PRESTo* software (Satriano et al., 2011), which incorporates the *RTLo*c algorithm for event location (Satriano et al., 2008). The IMR, located along the Eurasian–African plate boundary, is a tectonically complex area encompassing southern Iberia and northern Morocco and Algeria (Fig. 1a). Historically, the region has been affected by major earthquakes, including the Lisbon 1755, Torrevieja 1829, and Arenas del Rey 1884 events (Mezcua and Martínez-Solares, 1983; Buforn et al., 2015). Although seismic activity was moderate throughout much of the 20th century, it has increased over the past three decades, with notable

https://doi.org/10.5194/egusphere-2026-4270
Preprint. Discussion started: 23 July 2026


events including the Al Hoceima 2004 ($M_w$ 6.4; Stich et al., 2005), Lorca 2011 ($M_w$ 5.1; Pro et al., 2014), and Alboran Sea 2016 ($M_w$ 6.4; Buforn et al., 2017) earthquakes, several of which caused significant damage (Fig. 1a).

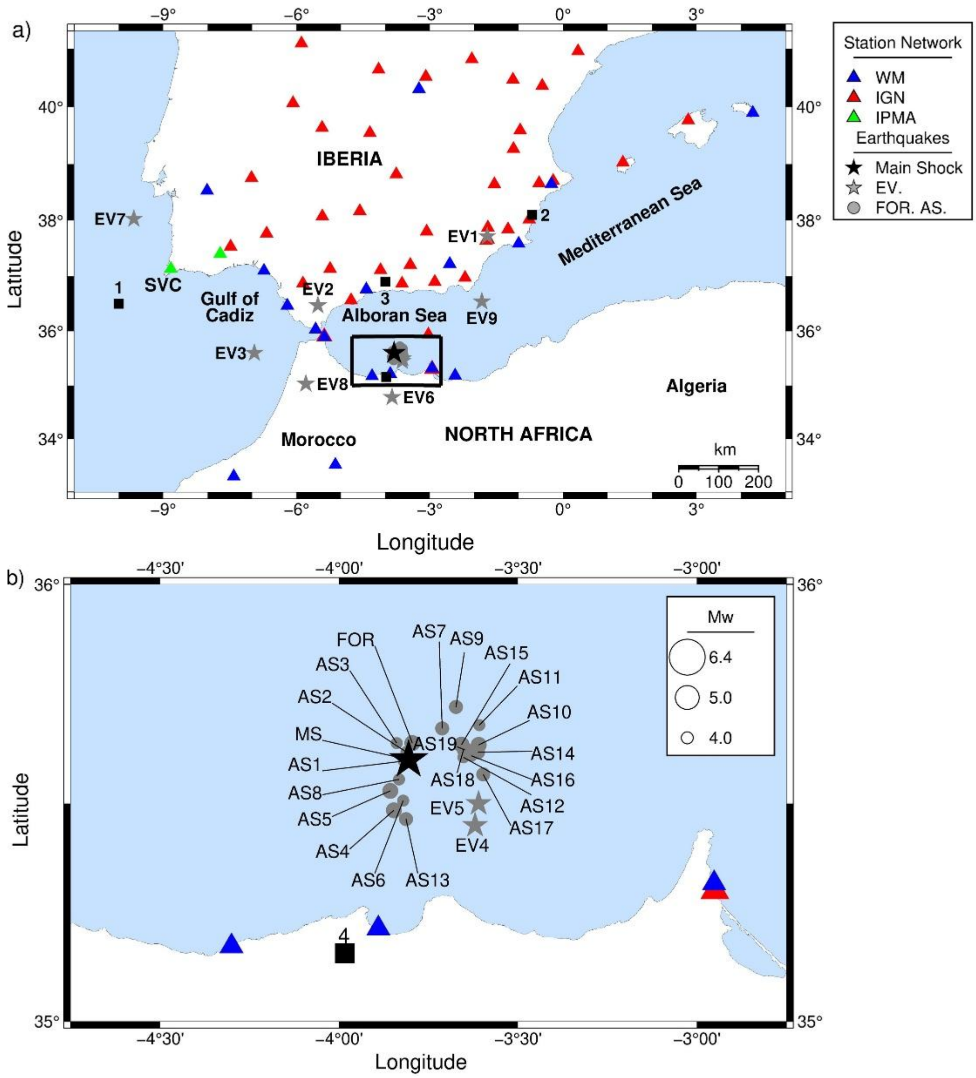


**Figure 1: (a)** Epicenters of the selected events for this study: EV1–EV9 are shown as gray stars, along with the mainshock (MS, black star), foreshock (FOR), and aftershocks (AS) of the 2016 Alboran seismic sequence with $M_w \geq 4$ (gray circles). Triangles indicate the broad-band seismic stations used: Western Mediterranean (WM, blue), *Instituto Geográfico Nacional* (IGN, red), and *Instituto Português do Mar e da Atmosfera* (IPMA, green). The boxed region marks the area shown in detail in panel b. **(b)** Zoomed-in view of the area highlighted by the box in panel (a). Symbol size is proportional to event $M_w$. 1: 1755 Lisbon earthquake $I_{max}$ X; 2: 1829 Torrevieja

https://doi.org/10.5194/egusphere-2026-4270
Preprint. Discussion started: 23 July 2026


earthquake $I_{max}$ IX-X; 3: 1884 Arenas del Rey earthquake $I_{max}$ IX-X; 4: 2004 Al Hoceima, $M_w$ 6.4; EV1: 2011 Lorca, $M_w$ 5.1; MS: 2016 Alboran Sea, $M_w$ 6.4. SVC: Cape St. Vincent.

While initial studies demonstrated *PRESTo*'s capability to provide reliable real-time earthquake early warning (Carranza, 2016; Carranza et al., 2013, 2017, 2021) in the IMR, UCM recently installed and tested a new software package called *QuakeUp* to enhance regional EEWS performance (Escudero et al., 2025). This platform implements the shaking-forecast-based early warning methodology described by Zollo et al., (2023), developed by the *RISSC-Lab* (*Unità di Ricerca in Sismologia Sperimentale e Computazionale*) at the *Università degli Studi di Napoli Federico II,* Italy. *QuakeUp* integrates onsite and network-based approaches, estimating source parameters through either the *RTLoc* (Satriano et al., 2008) or *MParLoc* (Zollo et al., 2021) algorithms for hypocentral location and OT determination, while applying the methodology of Zollo et al., (2023) for $M_w$ estimation. It predicts Peak Ground Velocity (PGV) by integrating observed P-wave amplitudes (onsite approach) with region-specific Ground Motion Prediction Equations (GMPE; network-based approach) using updated location and magnitude estimates. The software then provides continuous P-wave-based shakemaps expressed in terms of Instrumental Intensity ($I_{MM}$), calculated from PGV. This enables the real-time monitoring of the PDZ, which is defined as the areas where $I_{MM}$ exceeds a predefined threshold. Although the IMR is characterized by a low instrumentation density (Fig. 1) and a predominance of moderate-to-large-magnitude offshore earthquakes, *QuakeUp* has been shown to perform well in this region using the *RTLoc* earthquake location algorithm (Escudero et al., 2025). This performance is consistent with the long operational experience of *RTLoc* in the IMR, where it has been routinely used by *PRESTo* since its deployment and remains in operational use today (Carranza, 2016; Carranza et al., 2013, 2017, 2021). However, minimizing epicentral location errors is crucial for next-generation, shakemap-dependent frameworks like *QuakeUp*. Because the boundaries of a developing PDZ are defined by strict $I_{MM}$ thresholds, a mislocated epicenter can severely distort its shape and real-time evolution, resulting in dangerous missed or false alerts. We show that this vulnerability is a critical issue when forecasting shakemaps for the 2016 Alboran Sea seismic series.

Therefore, the primary objective of this study is to assess whether *MParLoc,* an alternative algorithm available in *QuakeUp*, can enhance earthquake localization performance and improve real time PDZ-based EEWS in the IMR. While *MParLoc* was previously validated on $M_w \geq 4.2$ earthquakes from the 2016-2017 Central Italy seismic sequence (Zollo et al., 2021), here we evaluate its performance within an operational EEWS framework in a region complicated by poor azimuthal station coverage, large azimuthal gaps for some regions such as the Saint Vincent Cape-Gulf of Cadiz and offshore seismicity and offshore seismicity. Particularly, we assess its impact on shaking forecasts and early-time location accuracy, which is a critical requirement for EEWS applications. To address this point, we focused on nine earthquakes with $M_w \geq 5$ that occurred in the IMR between 2011 and 2026 (EV1–EV9; Fig. 1). Additionally, to extend the early study of Escudero et al., (2025), we included the main shock ($M_w$ 6.4) and the 20 earthquakes with $M_w \geq 4$ from the 2016 Alboran Sea seismic series (MS, FOR and AS1-19, Fig. 1b). All events shown in Fig. 1 are listed in Table A1 and A2 (Appendix A).

https://doi.org/10.5194/egusphere-2026-4270
Preprint. Discussion started: 23 July 2026


To ensure consistency with an operational baseline, the reference locations used to test the two algorithms correspond to those reported by the *Instituto Geográfico Nacional* (IGN) earthquake catalogue (IGN, 2023). This choice allows a fair comparison between two real-time approaches rather than with refined, post-event solutions, such as those proposed by Lozano et al., 2025, for the 2016 Alboran Sea seismic series. Finally, because variations in earthquake localization directly influence the spatial positioning of developing PDZ maps, we perform real-time playback simulations for all selected events using both *RTLoc* and *MParLoc*. To fully explore the capabilities of the *MParLoc* algorithm, we test all possible combinations of its available observables (detailed in Sect. 2) against the IGN catalog baseline to identify the most suitable algorithm configurations for the IMR.

## 2 Methodology

In this study, we used the *QuakeUp* approach, which integrates earthquake detection and location, magnitude estimation, and PGV prediction. However, here we focus on the earthquake location module, which can employ the *RTLoc* (Satriano et al., 2008) and *MParLoc* (Zollo et al., 2021) algorithms. The general workflow of *QuakeUp* is shown in Fig. 2. For each event, the input consists of three-component velocity records from 62 broadband stations distributed across the IMR, with epicentral distances smaller than 700 km. The data were retrieved from the seismic networks of the IGN (IGN, 1999), Western Mediterranean (WM; ROA et al., 1996)), and the *Instituto Português do Mar e da Atmosfera* (IPMA; IMPA, 2006) (triangles in Fig. 1). P-wave arrivals are first identified on the vertical component using *Filter-Picker* algorithm (Lomax et al., 2012). Subsequently, following the approach of Caruso et al., (2017), a quality control procedure is applied to the input data. Once the earthquake is detected at 5 stations, an initial early-time location estimate of the hypocenter location and OT is provided using the *RTLoc* or *MParLoc* algorithms. This time is referred to as $T_{FIRST}$. These parameters are continuously updated as the P-wave arrivals are identified at additional stations. The time at which the final estimate is obtained is hereafter referred to as $T_{LAST}$. To reduce the dominant effect of noise at stations located at large epicentral distances, *QuakeUp* is configured to use only records from stations within 400 km of the first station that detects the earthquakes, as recently proposed by Escudero et al., (2025). With reference to the block diagram shown in Fig. 2, we briefly describe the methodology underlying each location algorithm. Further details can be found in the referenced studies.

https://doi.org/10.5194/egusphere-2026-4270
Preprint. Discussion started: 23 July 2026


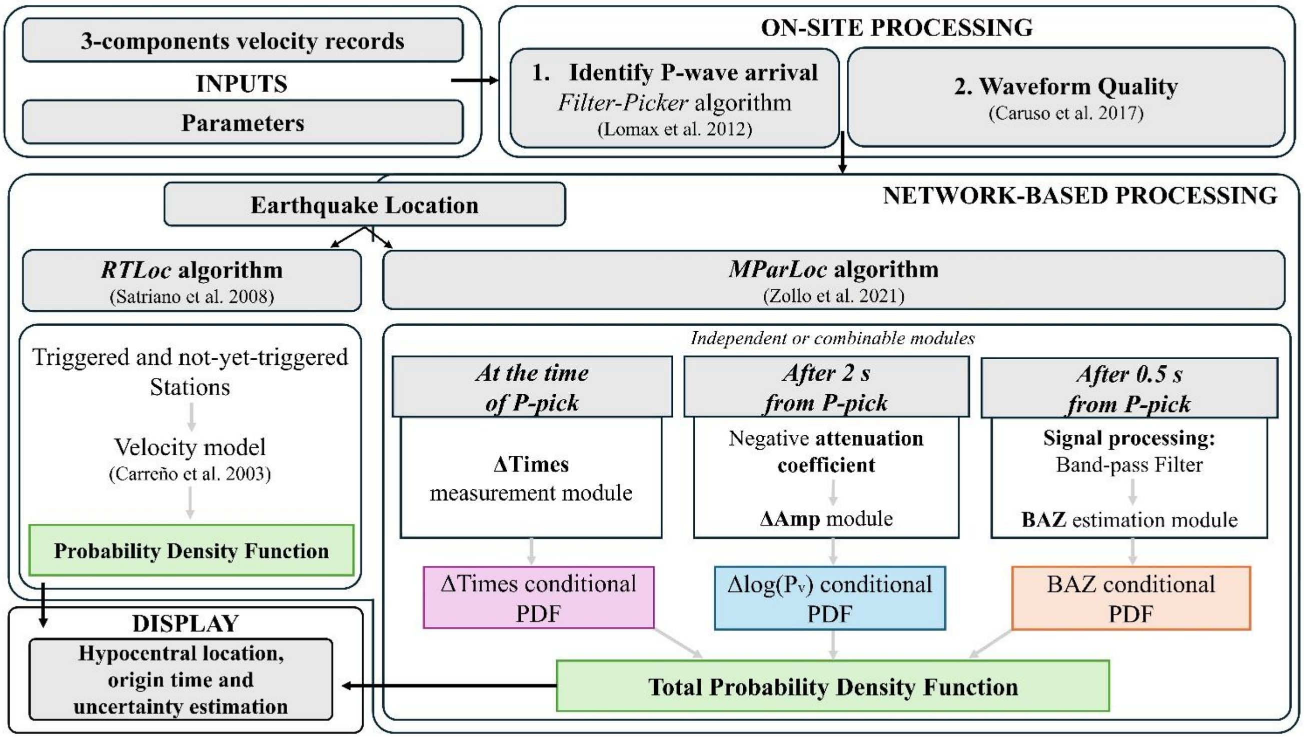


**Figure 2:** Block diagram of the location module implemented in *QuakeUp*. The upper panels illustrate the input data and the on-site processing performed at each individual station. The lower panel shows the earthquake location module (network-based processing), which can operate using two alternative algorithms: *RTLoc* (Satriano et al., 2008) (left panel) or *MParLoc* (Zollo et al., 2021) (right panel). For *MParLoc*, the workflow illustrates the sequential estimation of individual parameters, which are progressively combined and converge toward the final location solution (modified from Zollo et al., 2021).

The *RTLoc* algorithm (Satriano et al., 2008) uses, at each time step, both P-wave arrivals at triggered stations and the implicit constraints from non-triggered stations, allowing it to narrow possible source locations even when data are sparse. This method relies on the EDT formulation (Font et al., 2004), where each pair of stations defines an open surface of points with equal differential travel times to the two stations according to a velocity model (Satriano et al., 2008, 2013). The velocity model used for the IMR is described by Mezcua and Martínez-Solares (1983). Such a model was selected because it is the one used for the hypocentral locations reported in the IGN earthquake catalogue (IGN, 2022). This allows a more consistent comparison with the results obtained in this study. Furthermore, this same velocity model has been widely adopted in previous EEWS studies and applications within the IMR, where it has proven to be efficient (Carranza, 2016; Carranza et al., 2013, 2017, 2021; Escudero et al., 2025). Using this formulation, the algorithm minimizes the residual between theoretical and observed arrival times, incorporating information from both triggered and non-triggered stations. The earthquake is then located in the region where the largest number of EDT surfaces intersect (stack). This approach is robust to false P-picks,

https://doi.org/10.5194/egusphere-2026-4270
Preprint. Discussion started: 23 July 2026


which produce EDT surfaces that are inconsistent with the others and therefore do not contribute to the stack (Satriano et al., 2008, 2013). At each call, the *RTLoc* module provides (Fig. 2): (i) the probability density function (PDF) for earthquake location (obtained from the EDT stack), (ii) the most likely hypocenter and OT, and (iii) the covariance matrix representing spatial uncertainty of the earthquake location. These parameters are continuously updated as new real-time data are acquired, or simply as time evolves (Satriano et al., 2008, 2013).

The *MParLoc* algorithm (Zollo et al., 2021) employs an evolutionary Bayesian approach for real-time earthquake location, integrating information derived from multiple observables (ΔTimes, ΔAmp and BAZ) recorded at triggered stations. The procedures used to obtain these observables in real time are described below, while further details on the selection of optimal parameters for the IMR are provided in Appendix B.

**(1)** ΔTimes: In real-time operation, ΔTimes are computed as the time differences between the P-wave arrivals recorded at pairs of triggered stations. When more than two stations detect the P-wave, all possible station-pair combinations are evaluated and incorporated into the location procedure (Zollo et al., 2021).

**(2)** ΔAmp: At each triggered station, the P-wave peak velocity amplitude ($P_v$) is measured within a fixed 2 s time window following the P-wave arrival. Like the ΔTimes observable, the logarithm of the $P_v$ ratio is computed for every pair of stations where $P_v$ was recorded (Zollo et al., 2021). To apply the ΔAmp module, an empirical relationship specific to the IMR must be established, linking the measured $P_v$ values to the hypocentral distance ($R_{hypo}$, in km) and the $M_w$ of the events, expressed as:

$$\log_{10}P_v = A + B \cdot M_w + C \cdot \log_{10}R_{hypo} \quad (1)$$

where A, B and C are region-specific coefficients (Zollo et al., 2021). Since the ΔAmp module is based on amplitude ratios measured at different stations for the same event, the only coefficient in Eq. (1) that needs to be specified in the *QuakeUp* input parameters is C, the negative attenuation coefficient accounting for the decay of amplitude with distance (Fig. 2). In this work, the IMR-specific coefficients of Eq. (1) were determined using data from 28 earthquakes that occurred in the IMR between 2000 and 2024, with magnitudes $4.0 \leq M_w \leq 6.8$. A total of 2646 velocity records were obtained from seismic stations located at hypocentral distances ranging from 40 to 700 km (Appendix B, Table B1, and Fig. B1). Fig. 3a shows the $P_v$ values measured within the 2 s P-wave time window as a function of $R_{hypo}$. The color of each point corresponds to the $M_w$ of the earthquake. A least-squares fit on the measured data provided the IMR-specific coefficients for Eq. (1): A = –1.22, B = 0.66, C= –2.01, with a standard deviation (σ) of 0.43. The scattered behavior shown in Fig. 3a may reflect the intrinsic variability of the $P_v$– $R_{hypo}$

https://doi.org/10.5194/egusphere-2026-4270
Preprint. Discussion started: 23 July 2026


relationship (Eq. 1), as well as the influence of unmodeled factors such as local site effects and small-scale heterogeneities, given that a 1D attenuation medium is assumed. Nevertheless, the overall fit remains robust for the intended EEWS application.

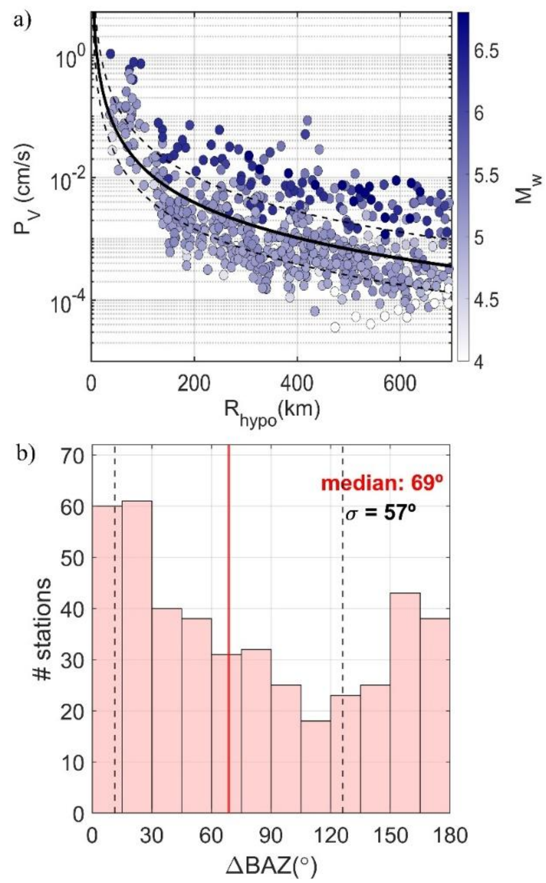


**Figure 3: (a)** Measured $P_v$ values in 2 s P-wave time windows as a function of hypocentral distance. The $M_w$ color bar (as reported in Table B1) is shown on the right. An $M_w$ of 5.5 was fixed to display the interpolated law (solid line) and its uncertainty (dashed line). **(b)** Histogram showing the ΔBAZs values for all selected events. The vertical red line marks the median value of the distribution, and the black dashed lines indicate the standard deviation.

**(3)** BAZ: The BAZ defined as the angle from North to the epicenter-to-station direction, is estimated within a 0.5 s P-wave time window at each triggered station. The BAZ calculation was performed by using the moving average approach, originally proposed by Nakamura (1988) and subsequently modified by Eisermann et al., (2015), as implemented in *QuakeUp* (Zollo et al., 2021, 2023). Initially, a polarization analysis is applied to the three-

https://doi.org/10.5194/egusphere-2026-4270
Preprint. Discussion started: 23 July 2026


component P-wave velocity traces, which are first band-pass filtered (Zollo et al., 2021). The filter frequency band is chosen to include the corner frequency ($f_c$) of each earthquake, which reflects the dominant frequency content of the source. This ensures that the analysis captures the most reliable portion of the P-wave energy, maximizes the signal-to-noise ratio, and allows the estimated polarization direction to accurately represent the propagation path from the epicenter to the station (Udías and Buforn, 2018). The $f_c$ for each event was calculated following the procedure described in Ap. The resulting $f_c$ values, along with the corresponding band-pass filter frequencies used for each event, are reported in Table B2 (Appendix B). Moreover, to resolve the 180° ambiguity inherent in BAZ measurements, the flip condition was applied. Fig. 3b presents a histogram of the differences between the BAZ estimated by *QuakeUp* at each station and the reference value for all selected events (ΔBAZ). The distribution shows a median of 69° and $\sigma = 57°$. Although BAZ estimates are subject to relatively higher uncertainty, they still provide useful constraints when combined with other observables (Zollo et al., 2021). Considering the large spatial extent of the IMR and its relatively sparse station coverage, differences of $\Delta BAZ \leq 30°$ are regarded as acceptable for location purposes. Under this criterion, 121 estimates fall within the 0°–30° range, whereas 81 estimates lie between 150° and 180°. The latter reflects the intrinsic 180° ambiguity in BAZ determinations, which is resolved in the location procedure through application of the flip condition.

For each independent observable – ΔTimes, ΔAmp and BAZ – a conditional PDF is computed. The total PDF is finally obtained by a Bayesian combination of the conditional PDFs of the selected modules, as shown in Fig. 2. This combination is flexible and depends on the observables that are available or deliberately included in the location process. Specifically, we evaluated four observable combinations: (i) ΔTimes, (ii) ΔTimes + ΔAmp, (iii) ΔTimes + BAZ, and (iv) ΔTimes +ΔAmp + BAZ. The method is evolutionary because, as the P-wavefront propagates across the seismic network and new data become available, the corresponding observables are progressively incorporated into the calculation. This leads to continuous updates of the total PDF, which is used to determine the maximum-likelihood solution for the earthquake hypocenter and OT, together with their associated uncertainties.

Finally, the differences in OT (ΔOT), epicenter location (ΔR), and depth (ΔZ) between the locations obtained using each algorithm available in *QuakeUp* (*RTLoc* and *MParLoc*) and those reported in the IGN Earthquake Catalogue (IGN, 2022) (Tables A1 and A2) were computed to better compare the performance of each algorithm. Location uncertainties are not explicitly analyzed in this study, as EEWS applications primarily focus on the location estimates themselves.

## 3 Results

Here we present a comparative analysis of the locations obtained with *RTLoc* (Satriano et al., 2008) and *MParLoc* (Zollo et al., 2021) for the selected events in the IMR (Fig. 1). The results are organized into three parts. Sect. 3.1. examines the performance of *RTLoc* versus *MParLoc* (ΔTimes + ΔAmp + BAZ) for the largest selected event, i.e., the $M_w$ 6.4 main shock

https://doi.org/10.5194/egusphere-2026-4270
Preprint. Discussion started: 23 July 2026


of the 2016 Alboran Sea seismic series (MS in Fig. 1). Sect. 3.2 compares the locations obtained at $T_{FIRST}$ and $T_{LAST}$ for all selected events (Fig. 1). Finally, Sect. 3.3 focuses on the Alboran Sea region, providing a detailed comparison of the temporal evolution of locations obtained with both algorithms, including the main shock and the 20 events with $M_w \geq 4$ from the 2016 seismic series (FOR and AS1–19; Fig. 1b).

In each section, results are presented for *RTLoc* and *MParLoc*. For the latter, we included the results for the configurations ΔTimes only and ΔTimes + ΔAmp + BAZ. Results for the ΔTimes + ΔAmp and ΔTimes + BAZ configurations are provided in Appendix C. Note that the ΔTimes configuration was specifically included because it relies on the same observables as *RTLoc* (P-wave arrival times), thereby enabling a direct comparison between the two algorithms. We also considered the ΔTimes + ΔAmp + BAZ combination because Zollo et al., (2021) reported that incorporating the additional observables (ΔAmp and BAZ) improves location accuracy compared with using arrival times alone. This improvement is particularly evident during the first few seconds of an event, when P-wave picks are sparse, or in networks with low station density or unfavorable geometries. This is directly relevant to the IMR, which, as mentioned earlier, has low instrumentation density and is dominated by moderate-magnitude offshore events (Fig. 1).

From this point onward, locations will be considered acceptable if they fall within the error limits proposed for the IMR (Carranza, 2016), specifically $\Delta R \leq 20$ km, $|\Delta Z| \leq 20$ km, and $\Delta OT \leq 5$ s.

### 3.1 Performance comparison of *RTLoc* and *MParLoc* for the Main Shock of the 2016 seismic series

The main shock of the 2016 Alboran Sea seismic series ($M_w$ 6.4, black star, Fig. 1b) occurred on 25 January 2016 at 04:22:01.53 UTC (OT) with a hypocenter located at 35.60°N, 3.81°W, and a depth of 12 km (IGN, 2022). Figures 4a-c show the temporal evolution of ΔR, ΔZ and ΔOT relative to the main shock OT for both *RTLoc* (black lines) and *MParLoc* (gray lines). For comparison, Fig. 4d illustrates how the number of parameters used in the location solutions varies over time.

https://doi.org/10.5194/egusphere-2026-4270
Preprint. Discussion started: 23 July 2026


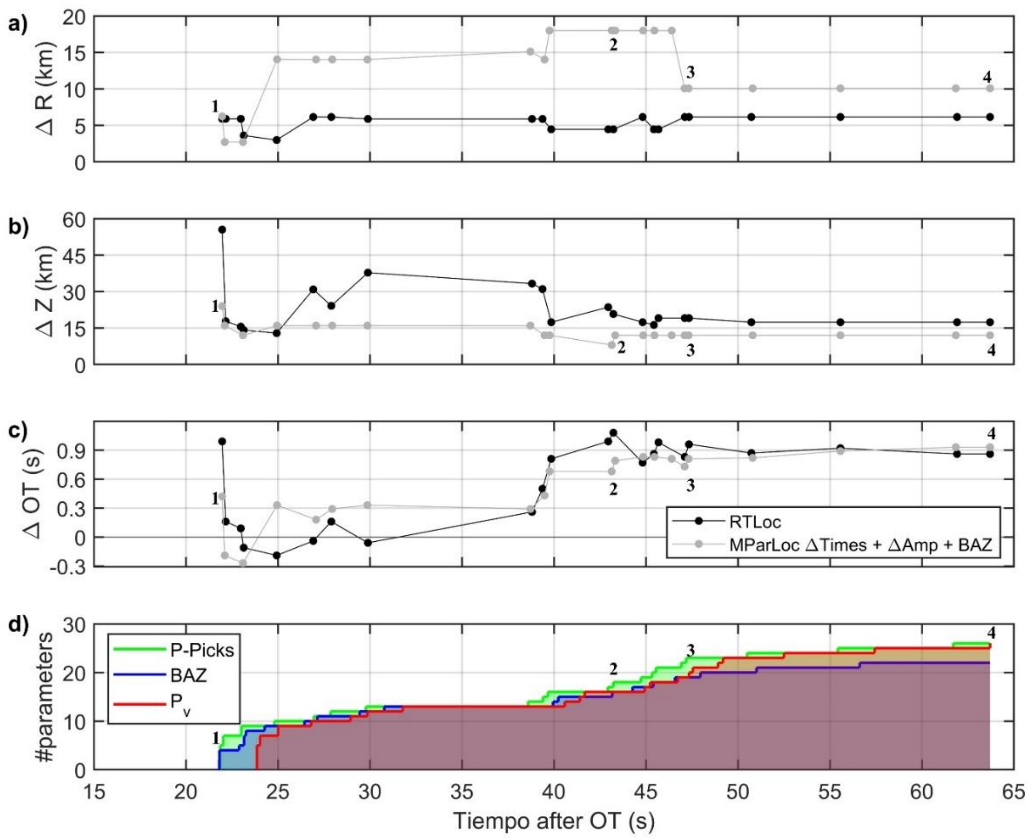


**Figure 4:** Temporal evolution of the performance of *RTLoc* (black lines) and *MParLoc* (ΔTimes + ΔAmp + BAZ, gray lines) for the main shock (MS, Fig. 1), expressed in terms of **(a)** ΔR, **(b)** ΔZ and **(c)** ΔOT. **(d)** Number of parameters used in the corresponding location solutions: the green indicates P-wave picks, blue for BAZ estimates, and red for $P_v$ measurements. Numbers indicate key time steps in the *MParLoc* evolution: 1) $T_{FIRST}$, 2) time at which ΔZ reaches a *plateau* value, 3) time at which ΔR reaches a *plateau* value, and 4) $T_{LAST}$.

We observe that $T_{FIRST}$ occurs 21.97 s after the OT for both algorithms (point 1 in Fig. 4). At this time, *RTLoc* uses a total of 5 P-picks, whereas *MParLoc* additionally incorporates 4 BAZ estimates. Including this additional information brings the first hypocentral location obtained with *MParLoc* closer to the reference value (IGN, 2022)). At the same time, ΔR is 6 km for both algorithms, while ΔOT is 0.40 s for *MParLoc* and 1.00 s for *RTLoc*. However, the main difference is observed in depth, where *MParLoc* achieves a ΔZ = 24 km compared to 56 km for *RTLoc*.

The ΔR values for both algorithms remain consistently below 20 km error limit (Fig. 4a). Two seconds after $T_{FIRST}$, *MParLoc* provides the epicentral estimate closest to the reference (ΔR=3 km), whereas *RTLoc* achieves similar accuracy 4 s after $T_{FIRST}$. Subsequently, the *MParLoc* ΔR fluctuates between 14 and 18 km until 47.11 s after the OT (point 3 in Fig. 4),

https://doi.org/10.5194/egusphere-2026-4270
Preprint. Discussion started: 23 July 2026


when it stabilizes at a 10 km *plateau*. During the same interval, *RTLoc* differences range from 4 to 6 km before stabilizing at a 6 km *plateau*. At this time, the solutions incorporate 23 P-picks, 19 BAZ estimates, and 19 $P_v$ values. The observed initial fluctuations in *MParLoc* may stem from the progressive inclusion of additional observables, which can introduce variability during early stages and highlight the trade-off between rapid solution updates and temporal stability.

Regarding depth estimation (Fig. 4b), the ΔZ value for *MParLoc* varies between 24 and 8 km from $T_{FIRST}$ until 43.33 s after the OT, eventually stabilizing at a 12 km *plateau* (point 2 in Fig. 4). At this point, the solution incorporates 18 P-picks, 16 BAZ estimates, and 16 $P_v$ values. For *RTLoc*, the initial ΔZ (Fig. 4b) drops rapidly to 17 km just 0.5 s after $T_{FIRST}$, then fluctuates between 13 and 30 km before reaching a stable 17 km *plateau* at 50.73 s after the OT based on 24 P-picks. While the *MParLoc* ΔZ values remain within the $|\Delta Z| \leq 20$ km limit at all times except for $T_{FIRST}$, the *RTLoc* exceeds this limit at $T_{FIRST}$ as well as between 26.92 and 43.23 s after the OT. In Fig. 4c, ΔOT ranges from −0.3 to 1.1 s for both algorithms, remaining well within the 5 s error limit. Moreover, discrepancies between the two algorithms remain minimal across all time step.

By $T_{LAST}$ (63.70 s after the OT; point 4 in Fig. 4), both algorithms yield estimates that closely match the reference values. At this time, a total of 26 P-picks and $P_v$ values, along with 22 BAZ estimates, are available. Incorporating these observables, *MParLoc* yields a ΔR of 10 km, a ΔZ of 12 km, and a ΔOT of 0.93 s, while *RTLoc* provides a ΔR of 6 km, a ΔZ of 17 km, and a ΔOT of 0.86 s.

### 3.2 Comparison of initial and final hypocentral locations for the selected earthquakes

To facilitate comparison of the hypocentral location accuracy, Figs. 5 and 6 show the spatial distribution of ΔR (upper panels) and ΔZ (lower panels) at $T_{FIRST}$ and $T_{LAST}$, respectively, across all selected events. These figures contrast the performance of *RTLoc* (Figs. 5a and 6a), *MParLoc* using only ΔTimes (Figs. 5b and 6b), and *MParLoc* using ΔTimes + ΔAmp + BAZ configuration (Figs. 5c and 6c). For completeness, additional results for the *MParLoc* configuration ΔTimes + ΔAmp and ΔTimes + BAZ are presented in Figs. C1 and C2. Furthermore, Supplementary Tables S1 and S2 compile the ΔR and ΔZ values obtained for each event by both *RTLoc* and all tested *MParLoc* configurations at both $T_{FIRST}$ and $T_{LAST}$.

https://doi.org/10.5194/egusphere-2026-4270
Preprint. Discussion started: 23 July 2026


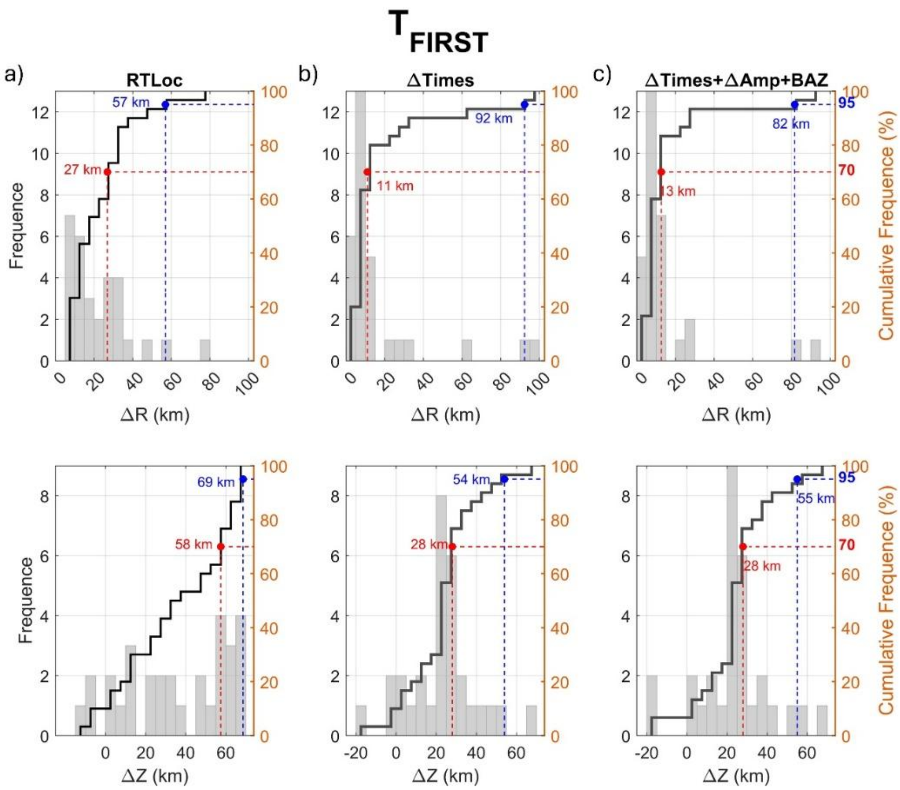


**Figure 5:** Comparison of algorithm performance at $T_{FIRST}$ using **(a)** *RTLoc,* **(b)** *MParLoc* ΔTimes only and **(c)** *MParLoc* with ΔTimes + ΔAmp + BAZ. The panels show histograms (gray) of ΔR (upper panels) and ΔZ (lower panels). In each panel, the black curve represents the cumulative histogram of the distribution, and the dashed vertical lines indicate the 70% (red) and 95% (blue) of the cumulative histogram.

Figure 5 shows that, at $T_{FIRST}$, *MParLoc* outperforms *RTLoc* in terms of hypocentral location accuracy, highlighting that the primary improvement provided by *MParLoc* occurs during the earliest stage of the EEWS process, when differences between both methods are most significant. Regarding epicentral location, the 70$^{th}$ percentile of the ΔR distribution is substantially lower when using *MParLoc* with ΔTimes only (11 km) or with ΔTimes + ΔAmp + BAZ (13 km), compared to *RTLoc* (27 km). Conversely, the 95$^{th}$ percentile is slightly lower for *RTLoc*. This latter result is primarily driven by a single event (AS7; Fig. 1), for which the maximum ΔR reaches 76 km. For *MParLoc* (both ΔTimes only and ΔTimes + ΔAmp + BAZ configurations), two events (EV6 and EV7) show ΔR values exceeding 80 km (Supplementary Table S1). Specifically, only 16 events fall within the $\Delta R \leq 20$ km error threshold using *RTLoc*, whereas 24 and 25 events satisfy this criterion when using *MParLoc* with ΔTimes only and with ΔTimes + ΔAmp + BAZ, respectively. In terms of depth, the 70$^{th}$ and 95$^{th}$ percentiles of the ΔZ distribution obtained with *RTLoc* are 58 km and 69 km, respectively. These values decrease to 28 km

https://doi.org/10.5194/egusphere-2026-4270
Preprint. Discussion started: 23 July 2026


and 54 km when using *MParLoc* with ΔTimes only, and to 28 km and 55 km when combining ΔTimes + ΔAmp + BAZ. For individual events, 9 *RTLoc* solutions satisfy the |ΔZ| ≤ 20 km error limit, whereas this number increases to 11 and 14 for *MParLoc* with ΔTimes + ΔAmp + BAZ and ΔTimes only, respectively.

When attention is focused on $T_{LAST}$, Fig. 6 indicates that all algorithms perform similarly, with only minor differences in the results. Regarding epicentral location, the 70$^{th}$ (and 95$^{th}$) percentiles of the ΔR distribution are comparable across the three approaches considered: 12 km (37 km) for *RTLoc*, 11 (31 km) and 16 km (35 km) for *MParLoc* with ΔTimes only, and with ΔTimes + ΔAmp + BAZ, respectively. At $T_{LAST}$, all *RTLoc* ΔR values fall below 40 km, whereas only a single event (EV7) exceeds this value under the other two *MParLoc* configurations (Supplementary Table S2). As a matter of fact, 11 events satisfy the ΔR ≤ 20 km threshold using *RTLoc*, compared to 24 and 25 events for the ΔTimes + ΔAmp + BAZ, and ΔTimes only *MParLoc* configurations, respectively. In terms of depth, the 70$^{th}$ percentile is similar across all three approaches, yielding 22 km for *RTLoc* and 20 km for both *MParLoc* configurations. The lowest 95$^{th}$ percentile is achieved by *MParLoc* with ΔTimes + ΔAmp + BAZ (29 km), whereas slightly higher values are obtained for *RTLoc* (38 km) and *MParLoc* with ΔTimes only (36 km). For individual events, 9 *RTLoc* solutions fall within the |ΔZ| ≤ 20 km error limit, compared to 13 events for *MParLoc* using ΔTimes only and 14 events for the full configuration (ΔTimes + ΔAmp + BAZ).

https://doi.org/10.5194/egusphere-2026-4270
Preprint. Discussion started: 23 July 2026


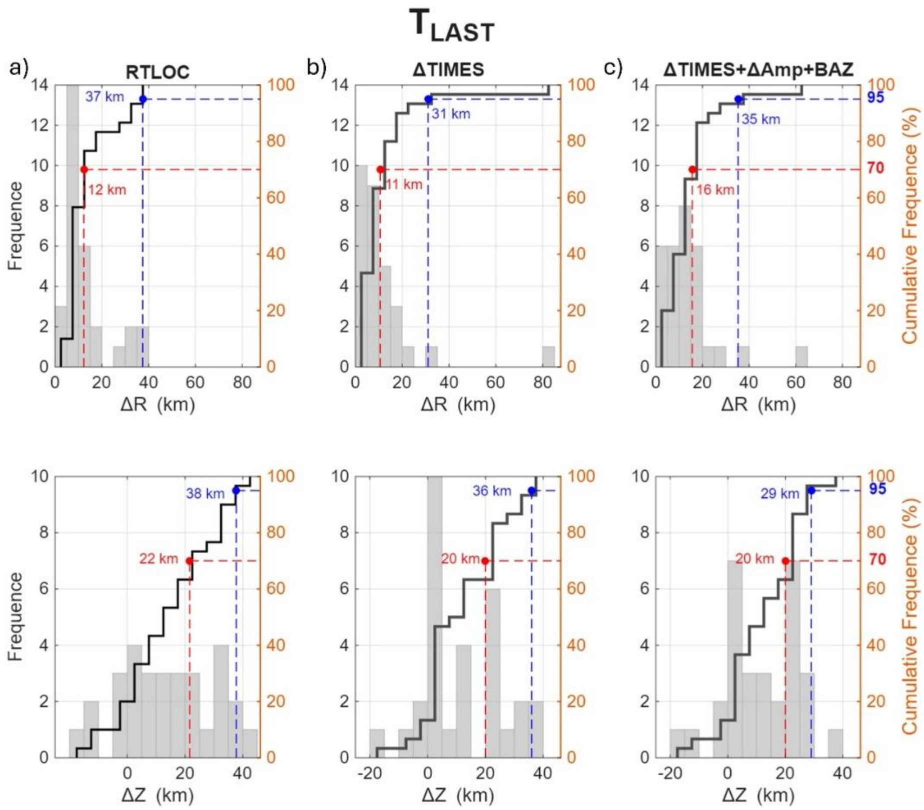


**Figure 6:** Comparison of algorithm performance at $T_{LAST}$ using **(a)** *RTLoc,* **(b)** *MParLoc* ΔTimes only and **(c)** *MParLoc* with ΔTimes + ΔAmp + BAZ. The panels show histograms (gray) of ΔR (upper panels) and ΔZ (lower panels). In each panel, the black curve represents the cumulative histogram of the distribution, and the dashed vertical lines indicate the 70% (red) and 95% (blue) of the cumulative histogram.

### 3.3 Time evolution of earthquake location accuracy for the 2016 Alboran Sea seismic series.

Focusing on the 2016 Alboran Sea seismic series ($M_w \geq 4$), we examined how the algorithms used in this study (*i.e.*, *RTLoc* and *MParLoc*) provide stable and reliable estimates of earthquake location parameters depending on the available data. Fig. 7 shows an aggregate plot of the evolution of location accuracy as a function of the number of available stations with recording P-arrival picks. These figures contrast three approaches, namely *RTLoc* (Fig. 7a), *MParLoc* using ΔTimes only (Fig. 7b), and *MParLoc* utilizing the full ΔTimes + ΔAmp + BAZ configuration (Fig. 7c). The results obtained using the remaining *MParLoc* configurations (ΔTimes + ΔAmp and ΔTimes + BAZ) are shown in Fig. D1 of Appendix D.

https://doi.org/10.5194/egusphere-2026-4270
Preprint. Discussion started: 23 July 2026


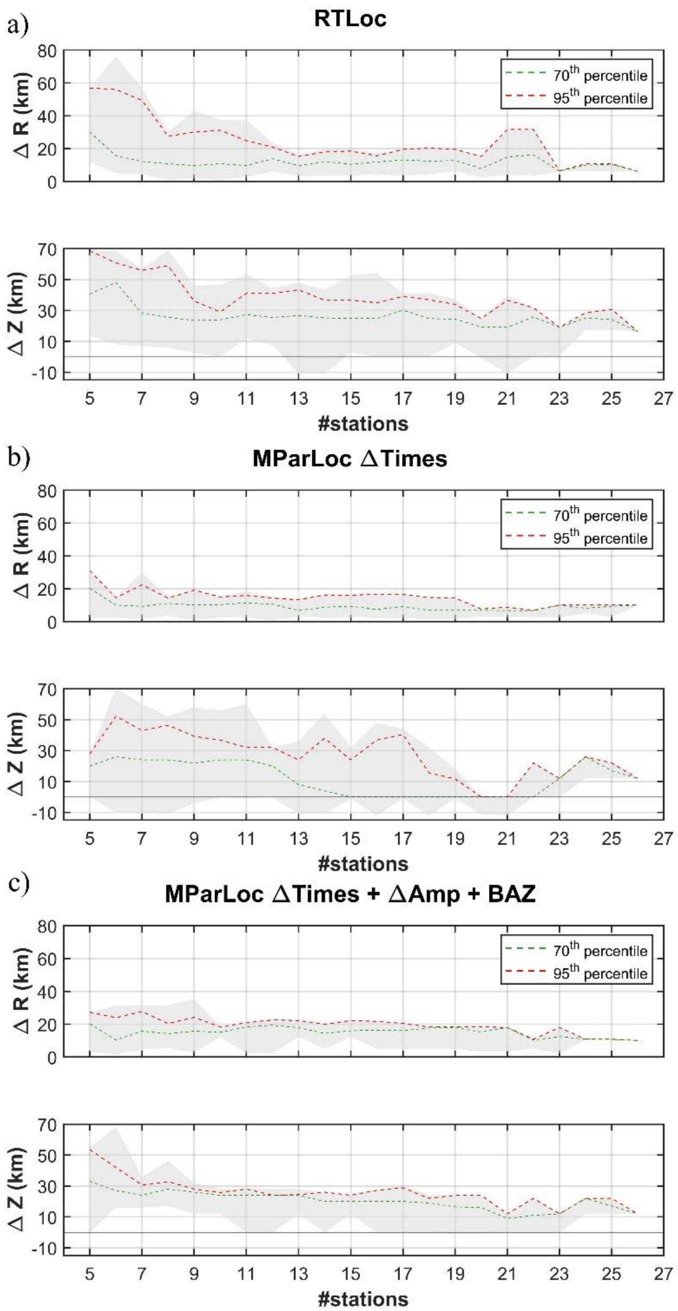


**Figure 7:** Aggregate plot of the evolution of location accuracy for the 2016 Alboran Sea seismic series events with $M_w \geq 4$ as a function of the number of P-picked stations, for three approaches: **(a)** *RTLoc* and *MParLoc*— **(b)** ΔTimes only and **(c)** ΔTimes + ΔAmp + BAZ. For each approach, the top and bottom panels show ΔR and ΔZ, respectively. The light gray area in each panel represents the dispersion curve. The green and red dashed lines correspond to the 70th and 95th percentiles, respectively.

https://doi.org/10.5194/egusphere-2026-4270
Preprint. Discussion started: 23 July 2026


Regarding the evolution of ΔR, Fig. 7a shows that the 70th percentile remains below the 20 km threshold starting from 6 stations when using *RTLoc*, and from 5 stations (i.e., $T_{FIRST}$) for *MParLoc* with ΔTimes only (Fig. 7b) and ΔTimes + ΔAmp + BAZ (Fig. 7c). However, when examining the evolution of the 95th percentile, all three approaches require a larger number of stations to drop below 20 km. For *RTLoc*, the 95th percentile stands at 57 km when 5 stations are used and decreases progressively, falling below 20 km from 12 stations onward. Notably, a secondary increase above 20 km occurs when 20–21 stations are involved. For the *MParLoc* configurations, the initial values are lower, yielding 31 km for ΔTimes only and 17 km for ΔTimes + ΔAmp + BAZ. The 95th percentile for the ΔTimes only configuration remains below 20 km from 8 stations onward, whereas the full ΔTimes + ΔAmp + BAZ variant securely settles below this limit from 12 stations onward.

Concerning the evolution of ΔZ, the 70th percentile for *RTLoc* (Fig. 7a) starts at 40 km with 5 stations and rises to a maximum of 48 km with 6 stations. From 7 stations onward, it decreases progressively, ranging from 30 km to 16 km, with the latter corresponding to the use of 26 stations. For *MParLoc* with ΔTimes only (Fig. 7b), the 70th percentile stays under 30 km and drops below 20 km from 12 stations onward, despite a local peak of 26 km at 24 stations. With the full ΔTimes + ΔAmp + BAZ configuration, the 70th percentile remains under 30 km, except for an initial value of 33 km at 5 stations, and falls below 20 km after 14 stations, showing a minor increase to 22 km at 24 stations. For the 95th percentile of ΔZ, *RTLoc* presents an initial value of 69 km with 5 stations, followed by a gradual decrease. However, ΔZ falls below 20 km only when more than 23 or 26 station are considered. For all other station counts, it remains above 20 km. For *MParLoc* with ΔTimes only, the 95th percentile starts at 28 km, rises to 52 km at 6 stations, and then decreases progressively. These values fall below 20 km from 18 stations onward, with secondary peaks of 22 km and 26 km at 22 and 24 stations, respectively. For *MParLoc* with ΔTimes + ΔAmp + BAZ, the 95th percentile begins at 54 km and decreases steadily, staying below 30 km from 9 stations onward and below 20 km at 21, 23, and 26 stations. Notably, the gray shaded region representing ΔZ is systematically narrower—and characterized by lower ΔZ values—when *MParLoc* is applied with ΔTimes + ΔAmp + BAZ, indicating significantly reduced data dispersion compared to the other configurations.

## 4 Discussion

The performance of the real-time earthquake location algorithms *RTLoc* (Satriano et al., 2008) and *MParLoc* (Zollo et al., 2021), both available in the *QuakeUp* software (Zollo et al., 2023), was assessed for events with $M_w \geq 4$ that occurred in the IMR between 2011 and 2026. Velocity records from broadband stations within the IMR, covering the areas of highest seismic hazard in the region (IGN, 2013), were used for the analysis.

The *RTLoc* algorithm, widely used in the IMR (Carranza, 2016; Carranza et al., 2013, 2017, 2021; Escudero et al., 2025), determines earthquake locations using absolute P-wave arrival times recorded at multiple seismic stations. In contrast,

https://doi.org/10.5194/egusphere-2026-4270
Preprint. Discussion started: 23 July 2026


*MParLoc*, whose performance in the IMR we aim to evaluate, can incorporate additional observables, such as ΔAmp and BAZ estimates, together with ΔTimes to locate earthquakes. To directly compare the performance of the two algorithms, location differences relative to the IGN reference solutions (IGN, 2022) were computed to assess whether incorporating these additional observables improves location accuracy.

The comparison was carried out at two key times. The first, $T_{FIRST}$, corresponds to the first earthquake location estimate obtained shortly after the earthquake's detection, when only 5 stations have reported P-wave arrivals and short P-wave time windows are available. This time is particularly relevant for EEWS applications, where obtaining a reliable location as quickly as possible is crucial. The second, $T_{LAST}$, corresponds to the final location obtained once all available parameters for each event have been incorporated.

Focusing on $T_{FIRST}$, where all events were constrained by 5 P-wave picks and between 2 and 5 BAZ estimates (Supplementary Table S1), we compared *RTLoc* with two different *MParLoc* configurations: ΔTimes alone and ΔTimes + ΔAmp + BAZ. For each event, we selected the solution that provides the most accurate location, *i.e.*, the one that minimizes the hypocentral distance difference (ΔHYP; Appendix E). Results indicate that *MParLoc* outperforms *RTLoc* in 77% of the events, regardless of the configuration used (ΔTimes alone or ΔTimes + ΔAmp + BAZ), whereas *RTLoc* provides the best solution in the remaining 23% (Fig. E1a–b). The improvement provided by *MParLoc* is mainly observed at early stages and should be interpreted in a statistical sense rather than as a systematic advantage for all events. We further evaluated the *MParLoc* configurations ΔTimes + ΔAmp and ΔTimes + BAZ (Fig. E1c–d), which outperform *RTLoc* in 83% and 73% of the events, respectively. Even when using only ΔTimes, *MParLoc* achieves higher location accuracy than *RTLoc*. This is because differential times leverage relative arrival differences between station pairs, yielding a larger number of independent constraints per event than absolute arrival times alone. Adding further observables, such as ΔAmp and BAZ estimates, enhances accuracy even more by providing complementary information about the source-station geometry and wave propagation. This improvement is especially significant at early times, when fewer observables are available, showing that including measurements beyond P-wave picks systematically enhances hypocentral location accuracy.

At $T_{LAST}$, *RTLoc* yielded the minimum ΔHYP for 37% of the selected events, while *MParLoc* provided the minimum ΔHYP for 63% of the cases, regardless of whether ΔTimes alone or ΔTimes + ΔAmp + BAZ were used (Fig. E2a–b). We also evaluated the *MParLoc* configurations ΔTimes + ΔAmp and ΔTimes + BAZ, which outperform *RTLoc* in 63% and 80% of the events, respectively (Fig. E2c–d). At this time, between 5 and 26 P-picks, 3 to 23 BAZ estimates, and 7 to 25 $P_v$ values were available for all events (Supplementary Table S2). The greater number of P-picks available at $T_{LAST}$ compared to $T_{FIRST}$ increases the number of independent constraints derived from absolute arrival times. As a result, the relative contribution of additional observables, such as ΔAmp and BAZ, becomes less pronounced. Although these parameters still provide complementary information on source-station geometry and wave propagation, their impact on refining hypocentral locations is diminished when the solution is already well-constrained by a large number of P-wave arrivals. This highlights

https://doi.org/10.5194/egusphere-2026-4270
Preprint. Discussion started: 23 July 2026


that the benefit of incorporating additional observables is most significant at early times, when fewer picks are available and differential measurements can substantially improve location accuracy.

Building on these observations, we further evaluated how the choice of earthquake location algorithm influences *QuakeUp*'s ground motion predictions, focusing specifically on the generation of $I_{MM}$-based shakemaps. These maps are derived from predicted PGV values using the empirical relationship of Faenza and Michelini (2010) and serve to track the evolution of the PDZ. This equation was selected due to its proven performance in the IMR. Specifically, Escudero et al., (2025) demonstrated that the resulting shakemaps are highly consistent with the macroseismic intensity maps reported in the IGN earthquake catalogue (IGN, 2022), validating its suitability for the present study.

The PGV values are predicted using two approaches (Zollo et al., 2023): the onsite approach, which is based on observed P-wave amplitudes and independent of the hypocentral location computed by *QuakeUp*, and the regional approach, which relies on region-specific GMPE that is updated as earthquake location and magnitude estimates evolve. For the specific case of the IMR, *QuakeUp* employs the GMPE proposed by Escudero et al., (2025). As a first approximation, if we neglect the effect of hypocentral location errors on $M_w$ estimates (see Appendix F), the location primarily affects the hypocentral distance term in the GMPE. Consequently, the variation in $I_{MM}$ ($\Delta I_{MM}$) resulting from differences in hypocenters obtained with *RTLoc* and *MParLoc* ($\Delta R_{hypo}$) can be computed as:

$$\Delta I_{MM} = \frac{1.82}{R_{hypo}} \Delta R_{hypo} \tag{2}$$

where $R_{hypo}$ is the reference hypocentral distance. Figure F1 shows the variation of $\Delta I_{MM}$, calculated using Eq. (2), as a function of $R_{hypo}$ (10–1000 km) for different $\Delta R_{hypo}$ values ranging from 5 to 50 km. As indicated by Eq. (2), larger $\Delta I_{MM}$ occur at small $R_{hypo}$ distances, and *vice versa*.

The following analysis addresses the impact of both algorithms on the shakemaps generated for the 2016 Alboran Sea seismic series. Notably, Escudero et al., (2025), in a dedicated study of *QuakeUp*'s performance during this sequence, found that the PDZ associated with the MS (Fig. 1) extended into North Africa, spanning approximately 40 to 100 km from the epicenter. This $R_{hypo}$ range is highlighted in Figure E1, demonstrating that differences in hypocentral location produce measurable changes in predicted intensities. For $\Delta R_{hypo\,=}$ 5–20 km, $\Delta I_{MM}$ ranges from 0 to 1, producing intensity variations of up to one class. For $\Delta R_{hypo\,=}$ 30–40 km, $\Delta I_{MM}$ ranges from 1 to 2 at the shorter $R_{hypo}$ (~ 40–60 km) and

https://doi.org/10.5194/egusphere-2026-4270
Preprint. Discussion started: 23 July 2026


decreases to 0–1 at 100 km. Finally, for $\Delta R_{hypo} =$ 50 km, $\Delta I_{MM}$ ranges from 2 to 3 at 40 km before decreasing to 0–1 at 100 km, which corresponds to intensity differences of up to three classes depending on $R_{hypo}$.

The $\Delta R_{hypo}$ values were calculated for the earthquakes of the 2016 Alborán Sea seismic series (MS, FOR, AS1-19, Fig.1). At $T_{FIRST}$, the median $\Delta R_{hypo}$ is 31 ± 17 km, which translates to a predicted $\Delta I_{MM}$ of 1 to 2 classes across $R_{hypo}$ distances of 40–100 km, and up to 3 classes for the largest $\Delta R_{hypo}$ values. By $T_{LAST}$, the median $\Delta R_{hypo}$ dops to 23 ± 12 km. This tighter constraint yields a smaller $\Delta I_{MM}$ and more reliable intensity forecasts, with differences typically limited to a single class. Ultimately, these findings clearly illustrate how improvements in hypocentral location from $T_{FIRST}$ to $T_{LAST}$ directly reduce uncertainties in $I_{MM}$ modeling.

To visualize these effects, Fig. 8 shows the $I_{MM}$-based shakemaps for events AS5 and AS7 at $T_{FIRST}$ (reported in each panel), computed using *RTLoc* and *MParLoc* with ΔTimes + ΔAmp + BAZ. The corresponding shakemaps at $T_{LAST}$, which reflect reduced location errors and more consistent intensity patterns, are presented in Figure F2.

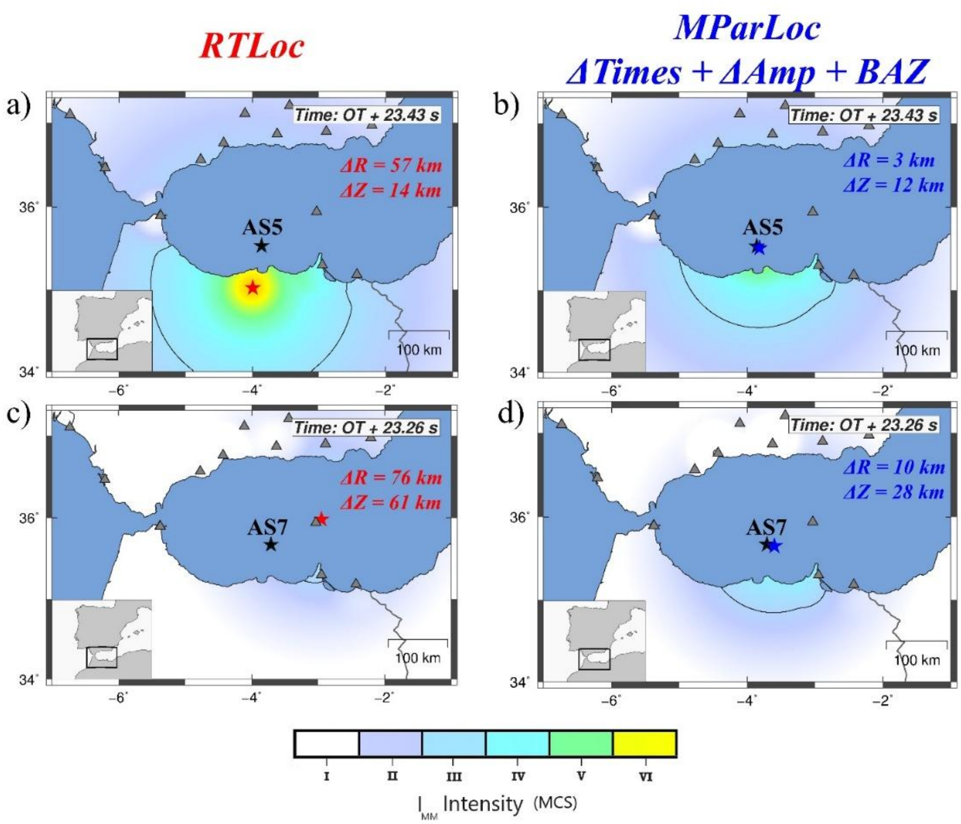


**Figure 8:** P-wave-based early shakemaps in terms of $I_{MM}$ based on the law of Faenza & Michelini (2010) for AS5 **(a** and **b)** and AS7 **(c** and **d)** at $T_{FIRST}$ (reported in each panel), using *RTLoc* (left) and *MParLoc* with ΔTimes + ΔAmp + BAZ (right). Stations are shown as

https://doi.org/10.5194/egusphere-2026-4270
Preprint. Discussion started: 23 July 2026


gray triangles, the black star indicates the IGN earthquake catalogue epicenters, and the red (blue) star marks the location obtained at $T_{FIRST}$ with *RTLoc* (*MParLoc*). ΔR and ΔZ values are reported for each case. The contour lines of the PDZ considering $I_{MM}^{thres}$=IV (Faenza & Michelini, 2010), are shown (black lines).

Focusing on the shakemaps at $T_{FIRST}$ for AS5 (Fig. 8a-b), the epicenter located by *RTLoc* (ΔR = 57 km, ΔZ = 14 km) shifts into northern Morocco, far from the reference epicenter. In contrast, the *MParLoc* solution (ΔR = 3 km, ΔZ = 12 km) is much closer to the reference location. By $T_{LAST}$ (Fig. S8a-b), both algorithms converge on locations highly similar to the reference point. In this instance, the $T_{FIRST}$ *RTLoc* location would have triggered numerous false alerts in Morocco. Its corresponding PDZ, defined by an $I_{MM}$ threshold of IV (light perceived shaking; Faenza and Michelini, 2010), extends widely, with predicted $I_{MM}$ values reaching up to VI (strong shaking; Faenza and Michelini, 2010) around the mislocated epicenter. Conversely, the *MParLoc* shakemap is significantly more robust, closely resembling the $T_{LAST}$ configurations of both algorithms with a PDZ that extends up to 100 km from the reference epicenter.

Similarly, the $T_{FIRST}$ shakemaps for AS7 (Fig. 8c-d) reveal a substantial difference between the two algorithms. *RTLoc* (ΔR = 76 km, ΔZ = 61 km) places the epicenter on the Moroccan coast, far from the reference location. By contrast, *MParLoc* (ΔR = 10 km, ΔZ = 28 km) locates the epicenter much closer to the reference point. By $T_{LAST}$ (Fig. S8c-d), both algorithms converge on locations nearly identical to the reference coordinates. For this event, the $T_{FIRST}$ *RTLoc* solution would have resulted in missed alerts in Morocco because the predicted PDZ barely extends into the region. Conversely, the *MParLoc* shakemap at $T_{FIRST}$ already captures the spatial distribution of intensity well, closely matching the final $T_{LAST}$ results with the PDZ extending up to 70 km from the reference epicenter. Overall, the comparison of AS5 and AS7 demonstrates the advantages of using *MParLoc* over *RTLoc*, particularly at $T_{FIRST}$ when differences between the two methods are most pronounced. In both cases, *RTLoc* at $T_{FIRST}$ exhibits substantial mislocations that lead to either false or missed alerts. By contrast, *MParLoc* produces epicentral locations much closer to the reference value. Consequently, *MParLoc* shakemaps better capture the spatial extent of the PDZ and closely resemble the final $T_{LAST}$ results, even during the earliest stages of the earthquake.

These examples (Fig. 8) highlight the practical impact of improved early-time location accuracy on EEWS performance. They demonstrate that incorporating additional observables into *MParLoc* can significantly enhance early-warning performance during the initial stages of an earthquake, providing longer and more reliable lead-times, which are critical for EEWS. Consequently, this study provides a regional-scale assessment of *MParLoc* within an operative EEWS framework, emphasizing its direct benefits for early warning systems.

https://doi.org/10.5194/egusphere-2026-4270
Preprint. Discussion started: 23 July 2026


## 5 Conclusions

In this study, we evaluated the performance of two earthquake location algorithms, *RTLoc* (Satriano et al., 2008) and *MParLoc* (Zollo et al., 2021), as implemented in the EEWS *QuakeUp* (Zollo et al., 2023), to assess whether the most recent developed *MParLoc* —which incorporates not only P-wave arrival times but also additional observables such as ΔAmp and BAZ estimates—can improve earthquake localization in the IMR, a region characterized by low station density and predominantly moderate-magnitude offshore earthquakes. Our key findings include:

(1) *MParLoc* generally improves earthquake location accuracy compared to *RTLoc*. For most of the analyzed events, *MParLoc* provides the minimum hypocentral distance difference relative to the IGN reference location.

(2) The improvements achieved by incorporating additional observables are greatest especially at early times after the earthquake detection ($T_{FIRST}$), when 5 stations and short time windows are available. This highlights the value of multi-parameter approaches for rapid earthquake characterization. However, at later times ($T_{LAST}$), the higher number of P-wave picks provides strong constraints on the location solution, reducing the relative contribution of other parameters (*i.e.* ΔAmp and BAZ estimates).

(3) Reducing location errors improves the reliability of $I_{MM}$-based shakemaps and the evolution of the PDZ. Because hypocentral location primarily affects the distance term in the GMPE used for regional PGV estimation, it directly shapes the resulting $I_{MM}$-based shakemaps. Incorporating ΔTimes, ΔAmp, and BAZ estimates secures a more robust earthquake characterization at $T_{FIRST}$. Consequently, *MParLoc*'s superior early location accuracy yields more reliable real-time shaking forecasts during the initial stages of the earthquake, reducing the time to first alert and increasing the lead-time for emergency safety actions inland.

Therefore, a PDZ-based EEWS with high-performance localization algorithm (such as *MParLoc*) would substantially improve warning capabilities in the IMR and generate high-value scientific and operational information. It would support the dissemination of precise alerts to the IGN and, subsequently, to Civil Protection and the Military Emergency Unit (*Unidad Militar de Emergencia*, UME), enabling faster responses and optimized resource deployment during seismic crises. Even in less favorable scenarios with limited lead-time, access to well-localized real-time PDZ maps would enable the immediate and precise mobilization of Civil Protection and UME resources, which is crucial for minimizing societal impacts.

## Appendix A

Tables A1 and A2 show the date, OT, hypocentral location (latitude, longitude, and depth), and moment magnitude ($M_w$) according to the IGN earthquake catalogue (IGN, 2022), for the selected events for the playback analysis (EV1-9, FOR, MS and AS1-19 in Fig. 1).

https://doi.org/10.5194/egusphere-2026-4270
Preprint. Discussion started: 23 July 2026


Table A1 includes earthquakes with $M_w \geq 5$ that occurred in the IMR during the 2011–2026 period (EV1-10), excluding events from the 2016 Alboran Sea seismic series. These excluded events are listed separately in Table A2, which provides information for the mainshock (MS), foreshock (FOR), and aftershocks (AS1-19) of the 2016 Alboran Sea seismic series ($M_w$ 4.0–6.4).

**Table A1.** Origin time, hypocentral coordinates, $M_w$ for earthquakes with $M_w$>5 that occurred in the IMR between 2011 and 2026.

| ID | Date | OT (UTC) | Lat. (ºN) | Lon. (ºE) | h (km) | $M_w$ |
|---|---|---|---|---|---|---|
| **EV1** | 11/05/2011 | 16:47:26.01 | 37.72 | -1.71 | 4f | 5.1 |
| **EV2** | 19/03/2013 | 03:11:31.50 | 36.47 | -5.52 | 43 | 5.1[c] |
| **EV3** | 16/12/2013 | 07:06:23.28 | 35.60 | -6.95 | 72 | 5.0[c] |
| **EV4** | 28/08/2021 | 11:20:50.07 | 35.45 | -3.62 | 0f | 5.1 |
| **EV5** | 20/05/2022 | 12:35:50.43 | 35.50 | -3.61 | 2 | 5.3 |
| **EV6** | 07/01/2023 | 08:12:26.37 | 34.78 | -3.85 | 3 | 5 |
| **EV7** | 26/08/2024 | 04:11:38.17 | 38.03 | -9.66 | 19 | 5.3 |
| **EV8** | 10/02/2025 | 22:48:42.81 | 35.03 | -5.79 | 34 | 5 |
| **EV9** | 14/07/2025 | 05:13:27.15 | 36.54 | -1.83 | 3 | 5.3 |

ID: Identifier. OT: Origin Time. h: depth (f: fixed).

[c]: $M_w$ values converted from MbLg (Cabañas et al., 2012)

**Table A2.** Origin time, hypocentral coordinates, $M_w$ for the mainshock, foreshocks, and aftershocks of the 2016 Alboran Sea seismic series ($M_w$ 4.0–6.4).

| ID | Date | OT (UTC) | Lat. (ºN) | Lon. (ºE) | h (km) | $M_w$ |
|---|---|---|---|---|---|---|
| **FOR** | 21/01/2016 | 13:47:19.45 | 35.64 | -3.80 | 0f | 5.1 |
| **MS** | 25/01/2016 | 04:22:01.53 | 35.60 | -3.81 | 12 | 6.3 |
| **AS1** | 25/01/2016 | 04:30:53.65 | 35.60 | -3.82 | 0f | 4.0[c] |
| **AS2** | 25/01/2016 | 04:34:18.62 | 35.62 | -3.82 | 0f | 4.4[c] |
| **AS3** | 25/01/2016 | 05:03:44.32 | 35.64 | -3.84 | 0f | 4.3[c] |
| **AS4** | 25/01/2016 | 05:54:04.51 | 35.48 | -3.85 | 0f | 5.2 |
| **AS5** | 25/01/2016 | 06:10:40.39 | 35.53 | -3.86 | 0f | 5.1 |
| **AS6** | 25/01/2016 | 08:25:04.06 | 35.51 | -3.82 | 0f | 4.4 |
| **AS7** | 25/01/2016 | 14:52:41.27 | 35.67 | -3.71 | 0f | 4.8 |
| **AS8** | 25/01/2016 | 18:17:32.13 | 35.56 | -3.83 | 0f | 4.1 |
| **AS9** | 27/01/2016 | 06:32:07.03 | 35.72 | -3.67 | 0f | 4.5 |
| **AS10** | 22/02/2016 | 03:46:03.14 | 35.63 | -3.61 | 12 | 5.1 |
| **AS11** | 23/02/2016 | 08:46:00.30 | 35.68 | -3.61 | 0f | 4.3 |
| **AS12** | 23/02/2016 | 10:12:32.13 | 35.61 | -3.65 | 0f | 4.1[c] |

https://doi.org/10.5194/egusphere-2026-4270
Preprint. Discussion started: 23 July 2026


| | | | | | | |
|---|---|---|---|---|---|---|
| **AS13** | 03/03/2016 | 11:36:26.15 | 35.46 | -3.81 | 2 | 4.7 |
| **AS14** | 09/03/2016 | 23:46:08.03 | 35.62 | -3.61 | 11 | 4.5 |
| **AS15** | 11/03/2016 | 04:16:48.29f | 35.64 | -3.66 | 0 | 5.0 |
| **AS16** | 11/03/2016 | 04:19:48.07 | 35.61 | -3.63 | 10 | 4.1[c] |
| **AS17** | 12/03/2016 | 15:04:05.70f | 35.57 | -3.60 | 0 | 4.8 |
| **AS18** | 12/03/2016 | 15:17:11.51 | 35.63 | -3.65 | 1 | 4.8 |
| **AS19** | 15/03/2016 | 04:40:40.14 | 35.62 | -3.65 | 11 | 5.2 |

Same as Table A1

## Appendix B

For the accurate performance of each module of the *MParLoc* algorithm in the IMR, it is essential to determine the optimal parameter settings which are included in the *QuakeUp* input parameter archive (Fig. 2). The following sections detail the procedures used to select the parameters for P-wave differential amplitudes module and the BAZ module.

### (1) P-peak amplitude ratios

For ΔAmp module, it is necessary to develop an empirical relation specific to the IMR that links the P-wave amplitude measured in a 2 s time-window ($P_v$) to the hypocentral distance of the stations ($R_{hypo}$) and the $M_w$ of the events, as expressed in Eq. (1) of the main text. The procedure used to derive the IMR-specific coefficients of Eq. (1) is described below.

We have selected 28 earthquakes that occurred in the IMR from 2000 to 2024 with $4.0 \leq M_w \leq 6.8$ (Table B1; red circles, Fig. B1). A total of 2646 velocity records of the three components are available from seismic stations between 40 and 700 km of hypocentral distance (triangles, Fig. B1). The records are first corrected by removing the mean value and the linear trend. The P-wave arrivals in the vertical components are manually picked. These records are then divided by the sensitivity of the instrument to obtain them in m/s. At this stage, the signal-to-noise ratio (SNR) of the vertical components is calculated. The maximum signal amplitude (in a 5 s window after P-wave arrival) is compared to the pre-event noise level (in a 5 s window before P-wave arrival) of each velocity vertical record (Carranza et al., 2013). Records from stations whose vertical component has an SNR > 5 are selected, as this threshold excludes very noisy data without overly restricting the database. Using this criterion, the number of records was reduced to 1992. To obtain the $P_v$ values, the 664 records corresponding to the vertical components were measured using 2 s P-wave time windows. Fig. 3a of the main text shows the obtained $P_v$ values as a function of $R_{hypo}$. The color of each point corresponds to the $M_w$ of the earthquake listed in Table B1. A least-squares fit was applied to the measured data to obtain the region-specific coefficients for Eq. 1. The resulting equation from this adjustment is as follows:

https://doi.org/10.5194/egusphere-2026-4270
Preprint. Discussion started: 23 July 2026


$$\log_{10} P_v = 1.22 + 0.66 \cdot M_w - 2.02 \cdot \log_{10} R_{hypo} \qquad \text{(B1)}$$

where $P_v$ is expressed in m/s and $R_{hypo}$ in km.

**Table B1.** Selected events to develop the empirical law for the IMR (Eq. B1).

| Date | Lat. (ºN) | Lon. (ºE) | h (km) | $M_w$ | Date | Lat. (ºN) | Lon. (ºE) | h (km) | $M_w$ |
|---|---|---|---|---|---|---|---|---|---|
| **06/08/2002** | 37.88 | -1.79 | 4[1] | 4.6[1] | **17/12/2009** | 36.44[5] | -9.93[5] | 38[5] | 5.5[5] |
| **21/05/2003** | 36.88[2] | 3.53[2] | 4[2] | 6.8[2] | **11/05/2011** | 37.72 | -1.71 | 4[7] | 5.1[7] |
| **29/07/2003** | 35.80[3] | -10.60[3] | 40[3] | 5.3[3] | **05/06/2012** | 36.86[8] | -10.51[8] | 38[8] | 4.0[8] |
| **24/02/2004** | 35.16 | -3.98 | 14[4] | 6.3[4] | **22/05/2014** | 35.70 | 0.22 | 16 | 5.0 |
| **25/02/2004** | 35.14 | -3.95 | 14[4] | 4.4[4] | **03/11/2014** | 35.02[8] | -11.32[8] | 38[8] | 4.8[8] |
| **25/02/2004** | 35.11 | -3.89 | 10[4] | 5.2[4] | **21/01/2016** | 35.70[9] | -3.69[9] | 3[9] | 5.1[9] |
| **27/02/2004** | 35.15 | -3.94 | 12[4] | 4.3[4] | **25/01/2016** | 35.63[9] | -3.75[9] | 7[9] | 6.4[9] |
| **07/03/2004** | 35.13 | -3.96 | 22[4] | 5.0[4] | **25/01/2016** | 35.50[9] | -3.77[9] | 6[9] | 5.2[9] |
| **04/12/2004** | 34.98 | -2.97 | 6 | 5.0 | **25/01/2016** | 35.50[9] | -3.75[9] | 5[9] | 5.1[9] |
| **29/08/2005** | 36.59[6] | -11.19[6] | 40[6] | 4.6[6] | **22/02/2016** | 35.71[9] | -3.59[9] | 3[9] | 5.1[9] |
| **10/08/2006** | 35.50[6] | -9.91[6] | 40[6] | 4.4[6] | **11/03/2016** | 35.69[9] | -3.62[9] | 3[9] | 5.0[9] |
| **12/02/2007** | 35.96[5] | -10.35[5] | 35[5] | 6.1[5] | **15/03/2016** | 35.68[9] | -3.66[9] | 5[9] | 5.2[9] |
| **09/01/2008** | 35.64[6] | -0.64[6] | 6[6] | 4.7[6] | **20/05/2022** | 35.54[10] | -3.64[10] | 2 | 5.3 |
| **06/06/2008** | 35.88[6] | -0.69[6] | 10[6] | 5.5[6] | **07/01/2023** | 34.78 | -3.85 | 3 | 5.0 |

ID: Identifier. h: depth (f: fixed)

No superindex: IGN earthquake catalogue [1]: Buforn et al., 2006 [2]: Yelles et al., 2004 [3]: Pro et al., 2013 [4]: Stich et al., 2005 [5]: Lozano et al., 2020 [6]: Stich et al., 2010 [7]: Pro et al., 2014 [8]: Custódio et al., 2016 [9]: Buforn et al., 2017
[10]: Lozano et al., 2025

https://doi.org/10.5194/egusphere-2026-4270
Preprint. Discussion started: 23 July 2026


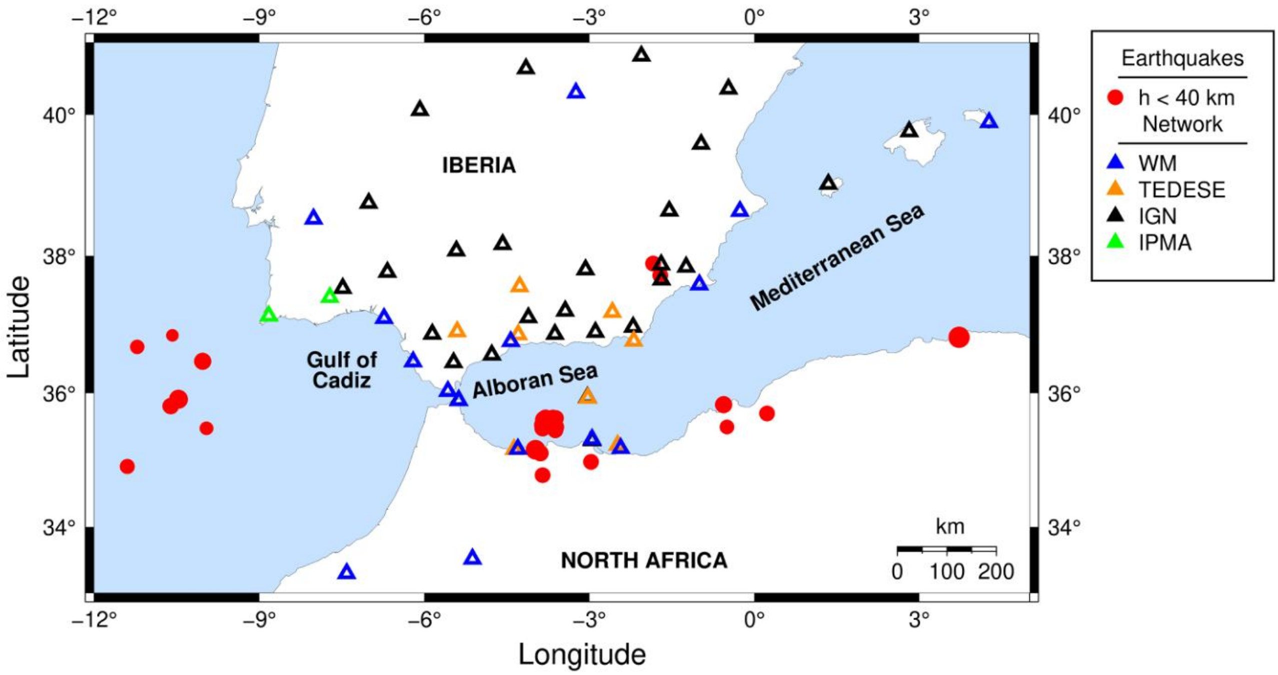


**Figure B1:** Earthquake epicenters (red circles, Table B1) and broadband stations (triangles) whose records were used to develop the empirical law specific to the IMR, with colors indicating the seismic network (blue WM, black IGN, green IPMA and orange TEDESE).

**(2) Back-azimuth**

This *MParLoc* module is based on BAZ estimation, which represents the angle from the North of the epicenter-to-station direction. It is estimated within 0.5 s P-wave time window (Zollo et al., 2021). A polarization analysis is then applied to the three-component P-wave amplitude signal after band-pass filtering. The band-pass filter frequencies were selected for each event according to the procedure described below.

First, the corner frequency ($f_c$) for each event was computed following Zollo et al., (2014), assuming a stress drop ($\Delta\sigma$) of 13.8 MPa (Yen et al., 2024). The resulting $f_c$ values for each event are reported in Table B2. Playback analyses were performed for each event using band-pass filters centered on $f_c$. The bands yielding the best location performance with *MParLoc* using BAZ only, to the reference locations, were selected and are reported in Table B2.

https://doi.org/10.5194/egusphere-2026-4270
Preprint. Discussion started: 23 July 2026


**Table B2**. $M_0$, $f_c$ and band-pass filter frequencies ($f_{min}$-$f_{max}$) used for the playback analysis of the selected earthquakes, as identified in
545 Tables S1 and S2.

| ID | $M_0$ (N·m) | $f_c$ (Hz) | $f_{min}$ (Hz) | $f_{max}$ (Hz) | ID | $M_0$ (N·m) | $f_c$ (Hz) | $f_{min}$ (Hz) | $f_{max}$ (Hz) |
|---|---|---|---|---|---|---|---|---|---|
| **EV1** | 5.6E+16 | 0.81 | 0.5 | 5.0 | **AS4** | 7.94E+16 | 0.72 | 0.4 | 4.0 |
| **EV2** | 5.6E+16 | 0.81 | 0.5 | 5.0 | **AS5** | 5.62E+16 | 0.81 | 0.5 | 5.0 |
| **EV3** | 4.0E+16 | 0.90 | 0.5 | 5.5 | **AS6** | 5.01E+15 | 1.80 | 1.5 | 5.0 |
| **EV4** | 5.62E+16 | 0.81 | 0.5 | 5.0 | **AS7** | 2.00E+16 | 1.14 | 0.8 | 5.5 |
| **EV5** | 1.12E+17 | 0.64 | 0.4 | 4.0 | **AS8** | 1.78E+15 | 2.55 | 0.5 | 5.0 |
| **EV6** | 4.0E+16 | 0.90 | 0.5 | 5.5 | **AS9** | 7.08E+15 | 1.61 | 1.0 | 4.5 |
| **EV7** | 1.1E+17 | 0.64 | 0.4 | 4.0 | **AS10** | 5.62E+16 | 0.81 | 0.5 | 5.0 |
| **EV8** | 4.0E+16 | 0.90 | 0.5 | 5.5 | **AS11** | 3.55E+15 | 2.03 | 0.5 | 5.0 |
| **EV9** | 1.1E+17 | 0.64 | 0.4 | 4.0 | **AS12** | 1.78E+15 | 2.55 | 1.5 | 5.0 |
| **FOR** | 5.62E+16 | 0.81 | 0.5 | 5.0 | **AS13** | 1.41E+16 | 1.28 | 1.0 | 4.5 |
| **MS** | 3.55E+18 | 0.20 | 0.1 | 2.0 | **AS14** | 7.08E+15 | 1.61 | 1.0 | 4.5 |
| **AS1** | 1.26E+15 | 2.86 | 0.5 | 5.0 | **AS15** | 3.98E+16 | 0.90 | 0.5 | 5.5 |
| **AS2** | 5.01E+15 | 1.80 | 1.5 | 5.0 | **AS16** | 1.78E+15 | 2.55 | 1.5 | 5.0 |
| **AS3** | 3.55E+15 | 2.03 | 1.5 | 5.0 | **AS17** | 2.00E+16 | 1.14 | 0.8 | 5.5 |
| **AS4** | 7.94E+16 | 0.72 | 0.4 | 4.0 | **AS18** | 2.00E+16 | 1.14 | 0.8 | 5.5 |
| **AS5** | 5.62E+16 | 0.81 | 0.5 | 5.0 | **AS19** | 7.94E+16 | 0.72 | 0.4 | 4.0 |

**Appendix C**

This section presents the histograms of ΔR and ΔZ at $T_{FIRST}$ and $T_{LAST}$ for the last two configurations (ΔTimes + BAZ and ΔTimes + ΔAmp), shown in Figs. C1 and C2, respectively, whereas the corresponding results for the other configurations
550 are presented in Figs. 5 and 6 of the main text. The ΔR and ΔZ values at $T_{FIRST}$ and $T_{LAST}$ for the selected events obtained with *RTLoc* and *MParLoc* under all tested observable combinations (ΔTimes only, ΔTimes + ΔAmp + BAZ, ΔTimes + ΔAmp, and ΔTimes + BAZ) are summarized in Supplementary Tables S1 and S2, respectively.

https://doi.org/10.5194/egusphere-2026-4270
Preprint. Discussion started: 23 July 2026


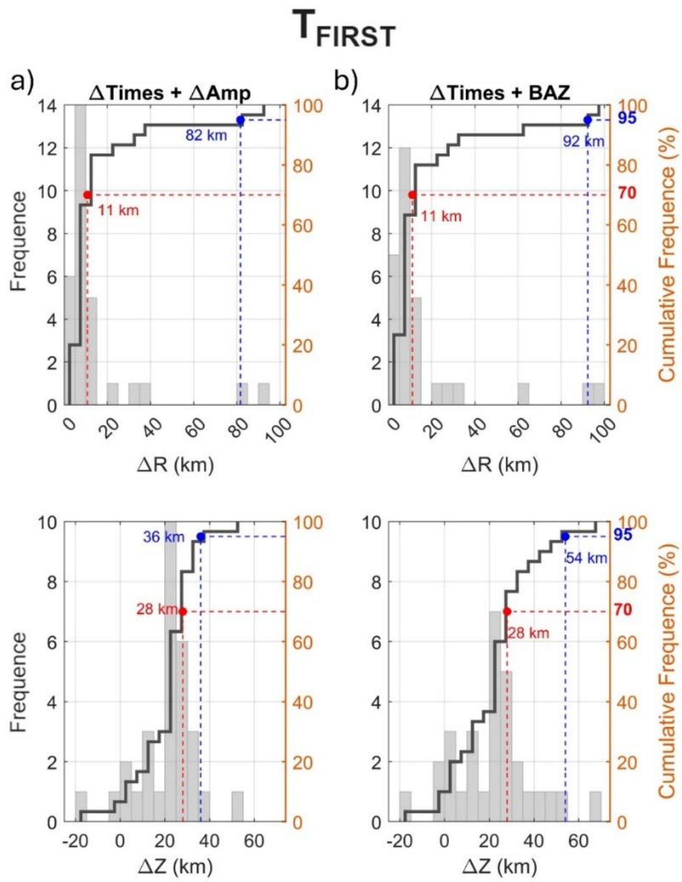


**Figure C1:** Comparison of algorithm performance at $T_{FIRST}$ using **(a)** *MParLoc* ΔTimes + ΔAmp and **(b)** ΔTimes + BAZ**.** The panels 555 show histograms (gray) of ΔR (upper panels) and ΔZ (lower panels). In each panel, the black curve represents the cumulative histogram of the distribution, and the dashed vertical lines indicate the 75% (red) and 95% (blue) of the cumulative histogram.

https://doi.org/10.5194/egusphere-2026-4270
Preprint. Discussion started: 23 July 2026


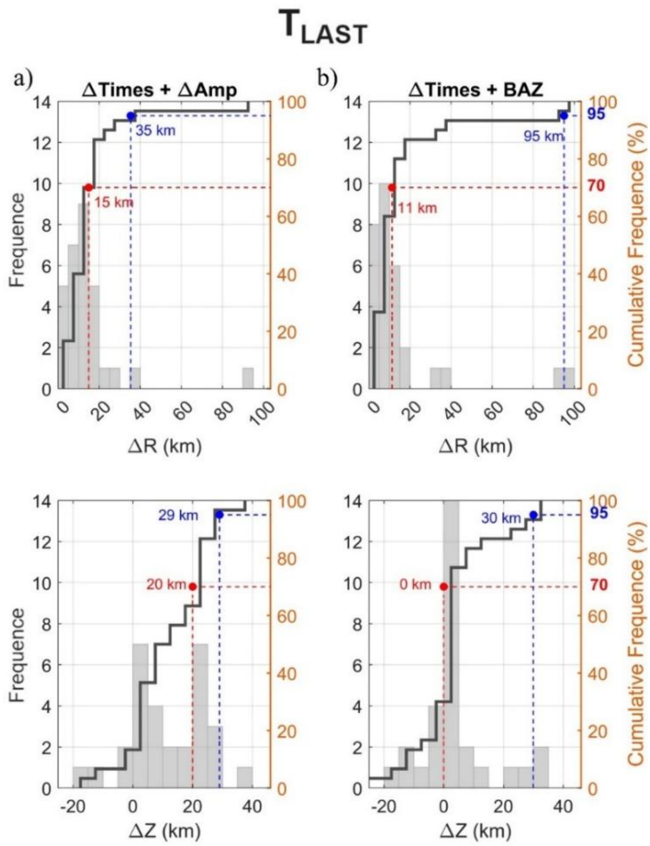


**Figure C2:** Comparison of algorithm performance at $T_{LAST}$ using **(a)** *MParLoc* ΔTimes + ΔAmp and **(b)** ΔTimes + BAZ**.** The panels show histograms (gray) of ΔR (upper panels) and ΔZ (lower panels). In each panel, the black curve represents the cumulative histogram of the
560 distribution, and the dashed vertical lines indicate the 75% (red) and 95% (blue) of the cumulative histogram.

## Appendix D

Figure D1 illustrates the evolution of hypocentral location accuracy for the 2016 seismic series events ($M_w \geq 4$) as a function of the number of available stations with P-picks, for two *MParLoc* configurations: ΔTimes + ΔAmp and ΔTimes + BAZ.

https://doi.org/10.5194/egusphere-2026-4270
Preprint. Discussion started: 23 July 2026


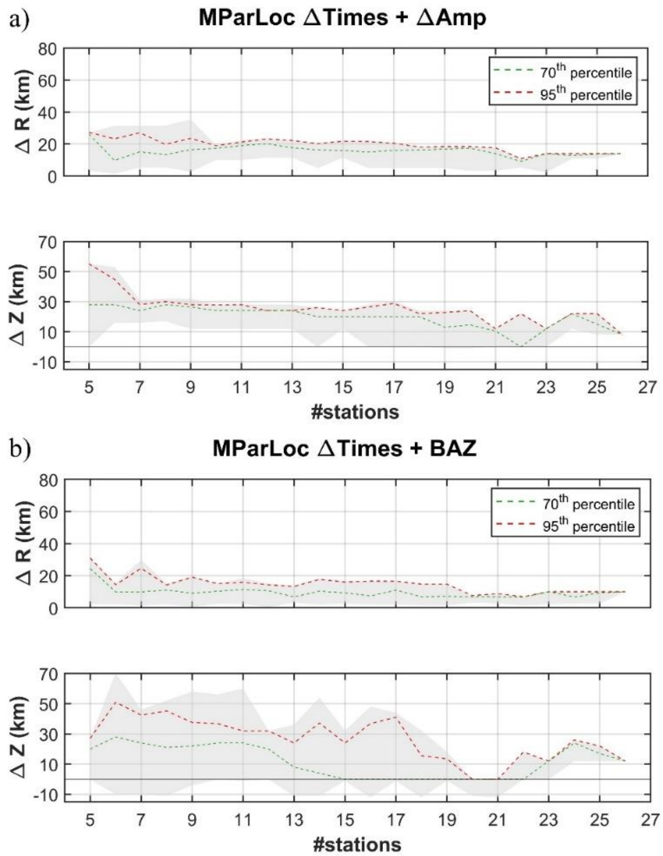


**Figure D1:** Aggregate plot of the evolution of location accuracy for the 2016 Alboran Sea seismic series events with $M_w \geq 4$ as a function of the number of P-picked stations, for two *MParLoc* configurations: **(a)** ΔTimes + ΔAmp and **(b)** ΔTimes + BAZ. For each approach, the top and bottom panels show ΔR and ΔZ, respectively. The light gray area in each panel represents the dispersion curve. The green and red dashed lines correspond to the 70th and 95th percentiles, respectively.

## Appendix E

This section provides a detailed comparison between *RTLoc* and *MParLoc* at $T_{FIRST}$ and $T_{LAST}$, considering all tested configurations. To determine the best-performing approach for each event at both $T_{FIRST}$ (Fig. E1) and $T_{LAST}$ (Fig. E2), we selected the configuration that minimizes the hypocentral distance difference (ΔHYP), defined as:

$$\Delta HYP = \sqrt{\Delta R^2 + \Delta Z^2} \tag{E1}$$

https://doi.org/10.5194/egusphere-2026-4270
Preprint. Discussion started: 23 July 2026


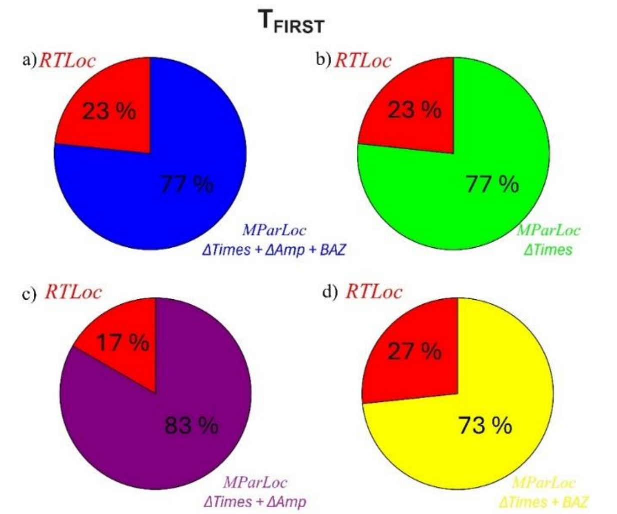


**Figure E1: (a)** Percentage of events for which the minimum ΔHYP at $T_{FIRST}$ is obtained with *RTLoc* (red) or *MParLoc* with ΔTimes + ΔAmp + BAZ (blue). **(b-d)** Same analysis as in **(a)** but considering *MParLoc* using ΔTimes only (green), ΔTimes + ΔAmp (purple), and ΔTimes + BAZ (yellow), respectively.

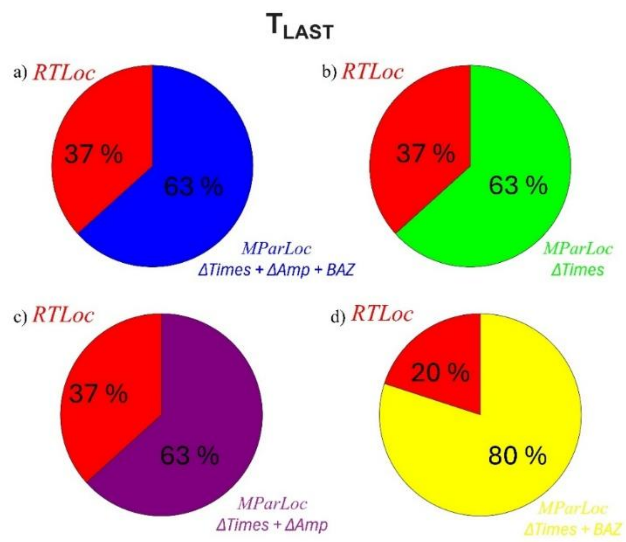


**Figure E2: (a)** Percentage of events for which the minimum ΔHYP at $T_{LAST}$ is obtained with *RTLoc* (red) or *MParLoc* with ΔTimes + ΔAmp + BAZ (blue). **(b-d)** Same analysis as in **(a)** but considering *MParLoc* using ΔTimes only (green), ΔTimes + ΔAmp (purple), and ΔTimes + BAZ (yellow), respectively.

https://doi.org/10.5194/egusphere-2026-4270
Preprint. Discussion started: 23 July 2026


**Appendix F**

In this section we analyze how differences between hypocentral locations obtained using *RTLoc* and *MParLoc* affect ground-shaking predictions in terms of Instrumental Intensity ($I_{MM}$).

*QuakeUp* continuously provides updated shakemaps expressed in terms of $I_{MM}$, computed from Peak Ground Velocity (PGV) using the empirical relationship proposed by Faenza and Michelini (2010):

$$I_{MM} = 5.1 + 2.3 \cdot 5\log(PGV) \quad \text{(F1)}$$

where PGV values are predicted using two approaches: (i) observed P-wave amplitudes (onsite approach), which is independent of hypocentral location, and (ii) region-specific GMPE (regional approach), updated as earthquake location and magnitude estimates evolve (Zollo et al., 2023). Within the IMR framework implemented in *QuakeUp*, the GMPE of Escudero et al., (2025) is used:

$$\log(PGV) = -2.78 + 0.99 \cdot M_w + 1.78 \cdot \log R_{hypo} \quad \text{(F2)}$$

where $R_{hypo}$ is the hypocentral distance in km. To study the effect of hypocentral location differences on predicted $I_{MM}$ values, we focus on their impact on the $R_{hypo}$ term in the GMPE. The earthquake $M_w$ is obtained by averaging magnitude estimates from multiple stations within expanding time windows (Zollo et al., 2023), which reduces its sensitivity to variations in hypocentral location. Therefore, we neglect the potential effect of location differences on $M_w$ and consider only their direct effect on $R_{hypo}$.

The variation in $I_{MM}$ ($\Delta I_{MM}$) resulting from differences between hypocenters obtained with *RTLoc* and *MParLoc* ($\Delta R_{hypo}$) can be computed as:

$$\Delta I_{MM} = \frac{\partial I_{MM}}{\partial R_{hypo}} \Delta R_{hypo} = \frac{1.82}{R_{hypo}} \Delta R_{hypo} \quad \text{(F3)}$$

where $R_{hypo}$ is the reference hypocentral distance. Figure F1 shows how $\Delta I_{MM}$ varies with $R_{hypo}$ for different $\Delta R_{hypo}$ values, as described by Eq. F3. Figure F2 presents *QuakeUp*-generated $I_{MM}$ shakemaps for AS5 (a, b) and AS7 (c, d) at $T_{LAST}$. The same shakemap results at $T_{FIRST}$ are shown in Fig. 8 of the main text.

https://doi.org/10.5194/egusphere-2026-4270
Preprint. Discussion started: 23 July 2026


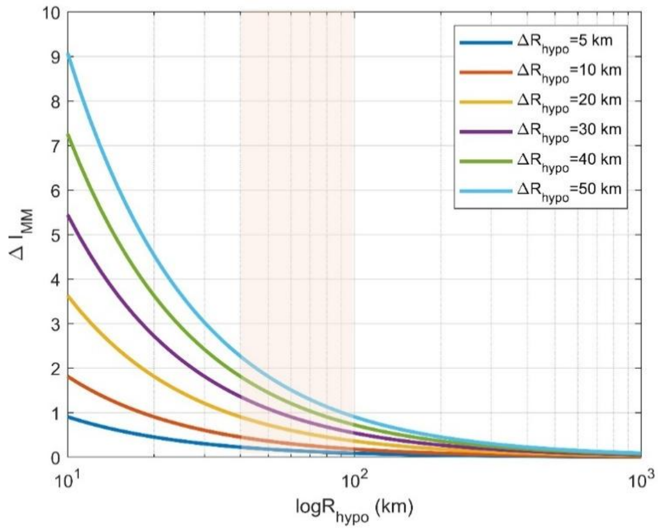


**Figure F1:** Variation of $\Delta I_{MM}$ with $R_{hypo}$ for different $\Delta R_{hypo}$ values. The range of $R_{hypo}$ from 40 to 100 km is shaded in orange.

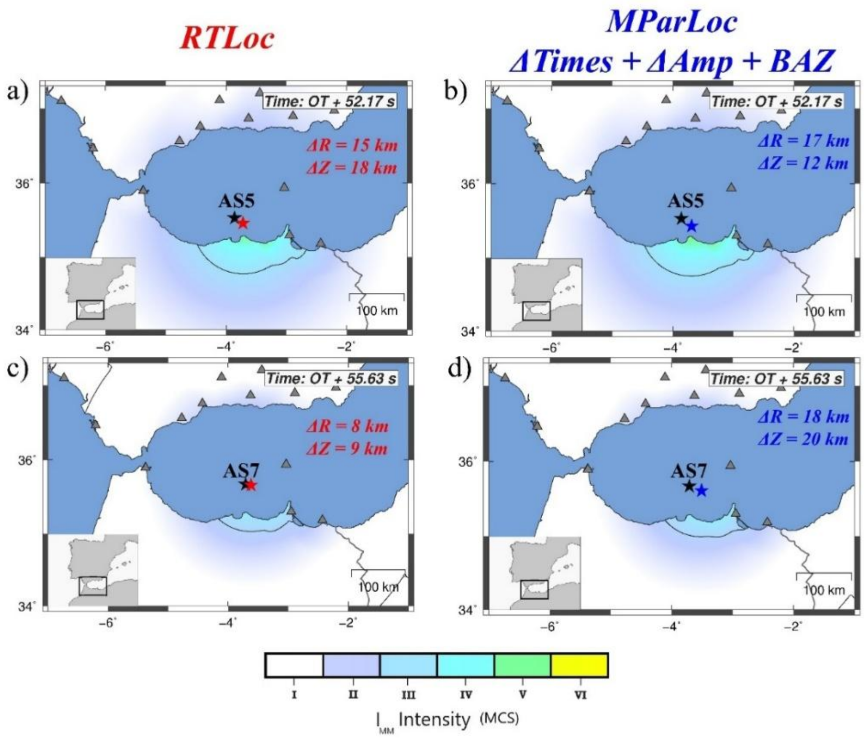


**Figure F2:** P-wave-based early shakemaps in terms of $I_{MM}$ based on the law of Faenza & Michelini (2010) for AS5 (**a** and **b**) and AS7 (**c** and **d**) at $T_{LAST}$ (reported in each panel), using *RTLoc* (left) and *MParLoc* with ΔTimes + ΔAmp + BAZ (right). Stations are shown as gray triangles, the black star indicates the IGN earthquake catalogue epicenters, and the red (blue) star marks the location obtained at $T_{LAST}$ with *RTLoc* (*MParLoc*). ΔR and ΔZ values are reported for each case. The contour lines of the PDZ considering $I_{MM}^{thres}$=IV (Faenza & Michelini, 2010), are shown (black lines).

https://doi.org/10.5194/egusphere-2026-4270
Preprint. Discussion started: 23 July 2026


## Code and data availability

The waveform data used for the playback analysis were obtained from seismic stations belonging to the IGN (IGN, 1999) and IPMA (IPMA, 2006) seismic networks, available through the Incorporated Research Institutions for Seismology (IRIS) Data Management Center (IRIS, 2026). Additional waveform data from the WM network (ROA et al., 1996) were provided by UCM. All the waveforms used for the calibration of the empirical law came from the same sources. The hypocentral locations and $M_w$ of selected earthquakes came from the IGN Earthquake Catalogue (IGN, 2022). These records were processed using Seismic Analysis Code, SAC (Version 101.6a, academic licence, available at http://ds.iris.edu/ds/nodes/dmc/software/downloads/sac/, last accessed, June 2024). The hypocentral locations and $M_w$ of selected earthquakes (Table A1, A2 and B1) came from published sources listed in the references and from the IGN seismic catalogue (IGN, 2022)

The used EEWS software (*QuakeUp*) can be found at https://www.prestoews.org/index.php (last accessed, February 2026). The grids to perform the location were calculated using the software *NLLoc* by A. Lomax, available at https://github.com/alomax/NonLinLoc (last accessed, January 2026), with a velocity model specific for the studied area (Caruso et al., 2017). The MATLAB code (24.1.0.2578822 (R2024a) Update 2, academic license) has been used for the calibration of empirical law. The same software was used to produce Figs. 3-7, C1, C1-E1. Figures 1, 8, B1 and E2 were made using Generic Mapping Tools Version 6.5.0 (https://docs.generic-mapping-tools.org/6.5/devdocs/team.html, last accessed, September 2024).

## Author contributions

**L. Escudero:** Conceptualization, Data curation, Formal analysis, Investigation, Methodology, Writing – original draft, Writing – review and editing. **M. Mattesini:** Conceptualization, Supervision, Validation, Writing – review and editing, Funding acquisition. **A. Zollo:** Conceptualization, Investigation, Validation, Methodology, Writing – review and editing. **G. de Landro:** Investigation, Validation, Methodology, Writing – review and editing. **L. Elia:** Software, Investigation, Validation, Methodology, Writing – review and editing. **E. Buforn:** Conceptualization, Investigation, Validation, Methodology, Writing – review and editing, Funding acquisition.

## Competing interest

The authors declare that they have no conflict of interest.

## Disclaimer

Copernicus Publications adds a standard disclaimer: “Copernicus Publications remains neutral with regard to jurisdictional claims made in the text, published maps, institutional affiliations, or any other geographical representation in this paper. While Copernicus Publications makes every effort to include appropriate place names, the final responsibility lies with the authors. Views expressed in the text are those of the authors and do not necessarily reflect the views of the publisher.” Please feel free to add disclaimer text at your choice, if applicable.

## Financial support

This work was partially supported by grants PID2021-122662OB-I00 and PID2025-168660OB-I00, funded by MICIU/AEI /10.13039/501100011033 and ERDF/UE, as well as by the “*Plan Propio UCM 2026, Convocatoria del programa de financiación de proyectos de investigación* (PR10/26-32654)". L. Escudero also gratefully acknowledges the PIPF-2024/COM-34266 fellowship from the regional government of the *Comunidad Autónoma de Madrid*.

## Review statement

The review statement will be added by Copernicus Publications listing the handling editor as well as all contributing referees according to their status anonymous or identified.

## References

Allen, R. M.: The ElarmS Earthquake Early Warning Methodology and Application across California, in: Earthquake Early Warning Systems, edited by: Gasparini, P., Manfredi, G., and Zschau, J., Springer, Berlin, Heidelberg, 13–21, https://doi.org/10.1007/978-3-540-72241-0_3, 2007.

Buforn, E., Udías, A., and Pro, C.: Large Earthquakes at the Ibero-Maghrebian Region: Basis for an EEWS, Pure Appl. Geophys., 172, 2387–2396, https://doi.org/10.1007/s00024-014-0954-0, 2015.

Buforn, E., Cesca, S., Goded, T., del Fresno, C., and Muñoz, D.: The Bullas (Murcia, SE Spain) earthquake, 29 January 2005, J. Seismol., 10, 65–72, https://doi.org/10.1007/s10950-006-2536-9, 2006.

Buforn, E., Pro, C., Sanz de Galdeano, C., Cantavella, J. V., Cesca, S., Caldeira, B., Udías, A., and Mattesini, M.: The 2016 south Alboran earthquake (Mw = 6.4): A reactivation of the Ibero-Maghrebian region?, Tectonophysics, 712, 704–715, https://doi.org/10.1016/j.tecto.2017.06.033, 2017.

https://doi.org/10.5194/egusphere-2026-4270
Preprint. Discussion started: 23 July 2026


Carranza, M., Buforn, E., Colombelli, S., and Zollo, A.: Earthquake early warning for southern Iberia: A P wave threshold-based approach, Geophys. Res. Lett., 40, 4588–4593, https://doi.org/10.1002/grl.50903, 2013.

Carranza, M.: Sistema de alerta sísmica temprana para el sur de la Península Ibérica: determinación de los parámetros de la alerta, Ph. D. thesis, Universidad Complutense de Madrid, Madrid, Spain, 2016 (in Spanish).

Carranza, M., Buforn, E., and Zollo, A.: Performance of a Network-Based Earthquake Early Warning System in the Ibero-Maghrebian Region, Seismol. Res. Lett., 88, 1499–1507, https://doi.org/10.1785/0220170081, 2017.

Carranza, M., Mattesini, M., Buforn, E., Zollo, A., and Torrego, I.: Four years of earthquake early warning in Southern Iberia: 2016–2019, Front. Earth Sci., 9, 696191, https://doi.org/10.3389/feart.2021.696191, 2021.

Cabañas, L., Rivas, A., Martínez-Solares, J. M., Gaspar-Escribano, J., Benito, B., Antón, R., and Ruiz-Barajas, S.: Preparación y homogeneización de un catálogo sísmico para la evaluación de la peligrosidad sísmica en España, Abstract, 7ª AHPGG, San Sebastián, Spain, 2012 (in Spanish).

Caruso, A., Colombelli, S., Elia, L., Picozzi, M., and Zollo, A.: An onsite alert level early warning system for Italy, J. Geophys. Res. Solid Earth, 122, https://doi.org/10.1002/2016JB01340, 2017.

Custódio, S., Lima, V., Vales, D., Cesca, S., and Carrilho, F.: Imaging active faulting in a region of distributed deformation from the joint clustering of focal mechanisms and hypocenters: Application to the Azores-Western Mediterranean region, Tectonophysics, 676, 70–89, https://doi.org/10.1016/j.tecto.2016.03.013, 2016.

Eisermann, A. S., Ziv, A., and Wust-Bloch, G. H.: Real-time back azimuth for earthquake early warning, Bull. Seismol. Soc. Am., 105, 2274–2285, https://doi.org/10.1785/0120140298, 2015.

Escudero, L., Zollo, A., Mattesini, M., Rea, R., Elia, L., Colombelli, S., and Buforn, E.: Performance of an Impact-Based Earthquake Early Warning System in the Alboran Sea, Seismol. Res. Lett., 96, 3063–3075, https://doi.org/10.1785/0220240474, 2025.

Faenza, L., and Michelini, A.: Regression analysis of MCS intensity and ground motion parameters in Italy and its application in ShakeMap, Geophys. J. Int., 180, 1138–1152, https://doi.org/10.1111/j.1365-246X.2009.04467.x, 2010.

Font, Y., Kao, H., Lallemand, S., Liu, C. S., and Chiao, L. Y.: Hypocentre determination offshore of eastern Taiwan using the Maximum Intersection method, Geophys. J. Int., 158, 655–675, https://doi.org/10.1111/j.1365-246X.2004.02317.x, 2004.

https://doi.org/10.5194/egusphere-2026-4270
Preprint. Discussion started: 23 July 2026


Incorporated Research Institutions for Seismology (IRIS) Data Management Center: IRIS Wilber 3, http://ds.iris.edu/wilber3/find_event/ (last access: January 2026), 2026.

Instituto Geográfico Nacional (IGN): Spanish Digital Seismic Network [data set], International Federation of Digital Seismograph Networks, https://doi.org/10.7914/SN/ES, 1999.

Instituto Geográfico Nacional (IGN): Actualización de mapas de peligrosidad sísmica de España 2012, Centro Nacional de Información Geográfica and Dirección General del Instituto Geográfico Nacional, Madrid, Spain, 2013 (in Spanish).

Instituto Geográfico Nacional (IGN): Spanish Earthquake catalogue [data set], https://doi.org/10.7419/162.03.2022, 2022.

Instituto Português do Mar e da Atmosfera (IPMA): Portuguese National Seismic Network [data set], International Federation of Digital Seismograph Networks, https://doi.org/10.7914/SN/PM, 2006.

Horiuchi, S., Negishi, H., Abe, K., Kamimura, A., and Fujinawa, Y.: An automatic processing system for broadcasting earthquake alarms, Bull. Seismol. Soc. Am., 95, 708–718, https://doi.org/10.1785/0120030133, 2005.

Liu, A., and Yamada, M.: Bayesian approach for identification of multiple events in an early warning system, Bull. Seismol. Soc. Am., 104, 1111–1121, https://doi.org/10.1785/0120130208, 2014.

Lomax, A., Satriano, C., and Vassallo, M.: Automatic picker developments and optimization: FilterPicker—A robust, broadband picker for real-time seismic monitoring and earthquake early warning, Seismol. Res. Lett., 83, 531–540, https://doi.org/10.1785/gssrl.83.3.531, 2012.

Lozano, L., Cantavella, J. V., and Barco, J.: A new 3-D P-wave velocity model for the Gulf of Cadiz and adjacent areas derived from controlled-source seismic data: application to nonlinear probabilistic relocation of moderate earthquakes, Geophys. J. Int., 221, 1–19, https://doi.org/10.1093/gji/ggz562, 2020.

Lozano, L., Buforn, E., Cantavella, J. V., López-Sánchez, C., Manzanedo, M. V., Barco, J., Antón, R., Cabieces, R., and Mattesini, M.: Relocation of recent shallow seismic activity in the Alboran Sea (Western Mediterranean Sea): the 2021–2024, 2016, and 2004 seismic series, Bull. Seismol. Soc. Am., 115, 469–488, https://doi.org/10.1785/0120240159, 2025.

Mezcua, J., and Martínez Solares, J. M.: Sismicidad en el área Ibero-Magrebí, Publicación Técnica No. 203, Instituto Geográfico Nacional, Madrid, Spain, 1983 (in Spanish).

Nakamura, Y.: On the urgent earthquake detection and alarm system (UrEDAS), in: Proceedings of the Ninth World Conference on Earthquake Engineering, Tokyo–Kyoto, Japan, II, 673–678, 1988.

Noda, S., Yamamoto, S., Sato, S., Iwata, N., Korenaga, M., and Ashiya, K.: Improvement of back-azimuth estimation in real-time by using a single station record, Earth Planets Space, 64, 305–308, https://doi.org/10.5047/eps.2011.10.005, 2012.

Pro, C., Buforn, E., Bezzeghoud, M., and Udías, A.: The earthquakes of 29 July 2003, 12 February 2007, and 17 December 2009 in the region of Cape Saint Vincent (SW Iberia) and their relation with the 1755 Lisbon earthquake, Tectonophysics, 583, 16–27, https://doi.org/10.1016/j.tecto.2012.10.010, 2013.

Pro, C., Buforn, E., Cesca, S., Sanz de Galdeano, C., and Udías, A.: Rupture process of the Lorca (southeast Spain) 11 May 2011 (Mw = 5.1) earthquake, J. Seismol., 18, 481–495, https://doi.org/10.1007/s10950-014-9421-8, 2014.

Rea, R., Colombelli, S., Elia, L., and Zollo, A.: Retrospective performance analysis of a ground shaking early warning system for the 2023 Turkey–Syria earthquake, Commun. Earth Environ., 5, 332, https://doi.org/10.1038/s43247-024-01507-3, 2024.

San Fernando Royal Naval Observatory (ROA), Universidad Complutense de Madrid (UCM), Helmholtz-Zentrum Potsdam Deutsches GeoForschungsZentrum (GFZ), Universidade de Évora (UEVORA, Portugal), and Institute Scientifique of Rabat (ISRABAT, Morocco): The Western Mediterranean BB Seismic Network [data set], Deutsches GeoForschungsZentrum GFZ, https://doi.org/10.14470/JZ581150, 1996.

Satriano, C., Lomax, A., and Zollo, A.: Real-time evolutionary earthquake location for seismic early warning, Bull. Seismol. Soc. Am., 98, 1482–1494, https://doi.org/10.1785/0120060159, 2008.

Satriano, C., Elia, L., Martino, C., Lancieri, M., Zollo, A., and Iannaccone, G.: PRESTo, the earthquake early warning system for southern Italy: Concepts, capabilities and future perspectives, Soil Dyn. Earthq. Eng., 31, 137–153, https://doi.org/10.1016/j.soildyn.2010.06.008, 2011.

Stich, D., Mancilla, F., Baumont, D., and Morales, J.: Source analysis of the Mw 6.3 2004 Al Hoceima earthquake (Morocco) using regional apparent source time functions, J. Geophys. Res., 110, B06306, https://doi.org/10.1029/2004JB003366, 2005.

Stich, D., Martín, R., and Morales, J.: Moment tensor inversion for Iberia–Maghreb earthquakes 2005–2008, Tectonophysics, 483, 390–398, https://doi.org/10.1016/j.tecto.2009.11.006, 2010.

https://doi.org/10.5194/egusphere-2026-4270
Preprint. Discussion started: 23 July 2026


Udías, A., and Buforn, E.: Principles of Seismology, Cambridge University Press, Cambridge, UK, ISBN 978-1-107-13869-8, 2018.

Wu, S., Yamada, M., Tamaribuchi, K., and Beck, J. L.: Multi-events earthquake early warning algorithm using a Bayesian approach, Geophys. J. Int., 200, 791–808, https://doi.org/10.1093/gji/ggu437, 2015.

Yelles, K., Lammali, K., Mahsas, A., Calais, E., and Briole, P.: Coseismic deformation of the May 21st, 2003, Mw = 6.8 Boumerdes earthquake, Algeria, from GPS measurements, Geophys. Res. Lett., 31, https://doi.org/10.1029/2004GL019884, 2004.

Zollo, A., Caruso, A., De Landro, G., Colombelli, S., and Elia, L.: A Bayesian method for real-time earthquake location using multiparameter data, J. Geophys. Res. Solid Earth, 126, e2020JB020359, https://doi.org/10.1029/2020JB020359, 2021.

Zollo, A., Colombelli, S., Caruso, A., and Elia, L.: An evolutionary shaking-forecast-based earthquake early warning method, Earth Space Sci., 10, e2022EA002657, https://doi.org/10.1029/2022EA002657, 2023.